AGU PUBLICATIONS

Geochemistry, Geophysics, Geosystems

RESEARCH ARTICLE
10.1002/2016GC006487

Ultra-high sensitivity moment magnetometry of geological samples using magnetic microscopy

Eduardo A. Lima[1] and Benjamin P. Weiss[1]

[1]Department of Earth, Atmospheric, and Planetary Sciences, Massachusetts Institute of Technology, Cambridge, Massachusetts, USA

Key Points:
- We describe measurements of samples with magnetic moments up to ~1000 times below the sensitivity of standard rock magnetometers
- Isolation of magnetic contamination in ultra-weak samples significantly improves accuracy compared to bulk moment measurements
- The accuracy is determined by the signal-to-noise ratio of the magnetic field maps and by the contribution from nondipolar magnetization

Supporting Information:
- Supporting Information S1
- Data Set S1

Correspondence to:
E. A. Lima,
limaea@mit.edu

Citation:
Lima, E. A., and B. P. Weiss (2016), Ultra-high sensitivity moment magnetometry of geological samples using magnetic microscopy, *Geochem. Geophys. Geosyst.*, *17*, 3754–3774, doi:10.1002/2016GC006487.

Received 13 JUN 2016
Accepted 31 AUG 2016
Accepted article online 8 SEP 2016
Published online 29 SEP 2016

Abstract Useful paleomagnetic information is expected to be recorded by samples with moments up to three orders of magnitude below the detection limit of standard superconducting rock magnetometers. Such samples are now detectable using recently developed magnetic microscopes, which map the magnetic fields above room-temperature samples with unprecedented spatial resolutions and field sensitivities. However, realizing this potential requires the development of techniques for retrieving sample moments from magnetic microscopy data. With this goal, we developed a technique for uniquely obtaining the net magnetic moment of geological samples from magnetic microscopy maps of unresolved or nearly unresolved magnetization. This technique is particularly powerful for analyzing small, weakly magnetized samples such as meteoritic chondrules and terrestrial silicate crystals like zircons. We validated this technique by applying it to field maps generated from synthetic sources and also to field maps measured using a superconducting quantum interference device (SQUID) microscope above geological samples with moments down to 10^{-15} Am^2. For the most magnetic rock samples, the net moments estimated from the SQUID microscope data are within error of independent moment measurements acquired using lower sensitivity standard rock magnetometers. In addition to its superior moment sensitivity, SQUID microscope net moment magnetometry also enables the identification and isolation of magnetic contamination and background sources, which is critical for improving accuracy in paleomagnetic studies of weakly magnetic samples.

1. Introduction

Until recently, the most sensitive magnetometers in the geosciences (i.e., the 2G Enterprises 755 Superconducting Rock Magnetometer (SRM)) were capable of measuring natural remanent magnetization (NRM) down to a limiting resolution of $\sim 1 \times 10^{-12}$ Am^2. In practice, background variations in the moment of sample holders will limit this to 1×10^{-8} Am^2 or even higher unless special precautions are taken to use nonmagnetic materials [*Kirschvink et al.*, 2015]. However, it has long been recognized that geological samples should be able to provide useful paleomagnetic records for moments at least several orders of magnitude below this threshold [*Kirschvink*, 1981]. These limitations in instrument sensitivity have been until recently the main factor determining the samples with the weakest magnetic moments that have been used for paleomagnetic measurements. For example, standard-sized (cm-scale) samples of lithologies with weak magnetizations ($\lesssim 10^{-3}$ Am^{-1}) like carbonates and lunar basalts, as well as smaller (~0.1 mm) samples of geological materials like single silicate crystals [*Sato et al.*, 2015; *Tarduno et al.*, 2015; R. R. Fu et al., Evaluating the paleomagnetic potential of single zircon crystals using the Bishop Tuff, preprint, arXiv:1605.08479, 2016] and chondrules [*Fu et al.*, 2014; *Lappe et al.*, 2013; *Lappe et al.*, 2011; *Uehara and Nakamura*, 2006] can have moments several orders of magnitude below 10^{-12} Am^2, particularly after laboratory demagnetization.

There have been several recent technological developments that currently or will soon enable higher sensitivity measurements. The recently developed small-bore 2G SRM has enabled measurements of moments down to $\sim 2 \times 10^{-13}$ Am^2 (D. Schuler, personal communication, 2016). Furthermore, ongoing efforts to develop a more sensitive bulk moment magnetometer using spin exchange relaxation free technology may lead to further improvements in sensitivity by 2 – 3 orders of magnitude for 1 cm^3 samples compared to the 2G SRM [*Dang et al.*, 2010].

Here we focus on another new ultra-high sensitivity technique for measuring the magnetic field above room temperature samples called superconducting quantum interference device (SQUID) microscopy (SM)

that has continuously developed over the last two decades [*Fong et al.*, 2005; *Weiss et al.*, 2007b]. By employing small (typically <100 μm) pickup loops brought extremely close to the samples, these instruments are capable of mapping the vertical component of the sample magnetic field with resolutions as low as 10 pT at spatial resolutions of 150 μm or better. Because the three components of the magnetic field measured in source-free space are interrelated by Gauss's Law and Ampère's Law, the two transverse field components can be uniquely calculated with high accuracy from these data, yielding the full vector field in a plane above the sample [*Lima and Weiss*, 2009].

The main application of this technique has been to infer the fine-scale magnetization distribution within geological samples [*Fu et al.*, 2012b; *Gattacceca et al.*, 2006; *Lima et al.*, 2013; *Oda et al.*, 2011; *Weiss et al.*, 2007a]. However, recovering magnetization distributions from field data is generally nonunique [*Baratchart et al.*, 2013; *Weiss et al.*, 2007b]. By comparison, magnetic field maps of a spatially unresolved (i.e., purely dipolar) sample can be used to uniquely retrieve the net magnetic moment of the source [*Lima et al.*, 2006; *Weiss et al.*, 2007b]. Our initial demonstrations of this approach have already established that moments as weak as 10^{-13} to 10^{-14} Am^2 can be retrieved, with the moments of relatively strongly magnetized samples obtained from SQUID microscopy and standard SQUID rock magnetometry in agreement [*Weiss et al.*, 2007b, 2008]. Furthermore, we recently successfully applied this technique as part of a comprehensive study of chondrules isolated from primitive chondritic meteorites that provided the first reliable paleointensities of fields in the solar nebula [*Fu et al.*, 2014], and to zircons from Bishop Tuff that provided accurate paleointensity measurements of the recent geomagnetic field (R. R. Fu et al., Evaluating the paleomagnetic potential of single zircon crystals using the Bishop Tuff, preprint, arXiv:1605.08479, 2016).

Here we present the first comprehensive demonstration of the accuracy and utility of this technique, its computational methodology and limitations, and its application to a typical paleomagnetic measurement suite involving progressive demagnetization. We begin in section 2 by demonstrating that samples with moments at least 100 times weaker than those detectable with standard SQUID rock magnetometers contain paleomagnetically meaningful information. Having demonstrated why we are developing the moment magnetometry technique for ultrasensitive instruments like SQUID microscopes, we describe the technique in section 3. Then, in section 4, we characterize its performance by applying it to controlled magnetization distributions for synthetic samples. We then validate the technique in section 5 using natural samples and comparison to measurements from standard rock magnetometers. We conclude that section with application of the technique to the measurement of samples that are inaccessible to standard rock magnetometers, demonstrating the detection of moments as weak as 1×10^{-15} Am^2.

2. The Need for Ultra-High Sensitivity Moment Magnetometry

We begin by using a simple analysis to demonstrate that there should be paleomagnetically meaningful information carried by ferromagnetic grain assemblages with moments well below 10^{-12} Am^2. In particular, we estimate the smallest magnetic moment for a grain assemblage that would accurately constrain the paleointensity or the paleodirection of an ancient magnetizing field $\boldsymbol{B}$. The error in the recorded paleodirection is defined as the angle between the net moment (i.e., resultant) of the assemblage and the ancient field direction. The error in paleointensity is defined as the fractional deviation of the efficiency, e (i.e., ratio of the net moment to the saturation moment), relative to that typically observed for large numbers of grains. We consider two different paleofield strengths that produce $e = 0.015$ and 0.15, which empirically are observed for typical grain assemblages carrying a thermoremanence acquired in fields B of 50 and 500 μT, respectively [*Yu*, 2010].

We consider an assemblage of identical single domain magnetite crystals with uniaxial anisotropy and spontaneous magnetic moments M_s with orientations distributed uniformly across the surface of the unit sphere. An extreme lower limit on the weakest most useful magnetic moment is set by the spontaneous moment of one spherical single domain grain with radius just above the superparamagnetic threshold ($\sim$25 nm) [*Butler and Banerjee*, 1975], for which $m \sim 3 \times 10^{-17}$ Am^2. Because this grain can be magnetized only in two directions and always has the same spontaneous moment intensity, it can record paleofield directions with errors up to 90° and essentially cannot record paleointensities.

To obtain a more meaningful lower limit, we use a Monte Carlo simulation to estimate the minimum number of grains, $n_{\min}$, that must be measured to achieve on average an angular error of $\overline{\theta_e} = 10°$ in the paleofield direction $\hat{B}$ and an error in the paleofield intensity of $\overline{m_e} = 20\%$. We can see that for this uniform

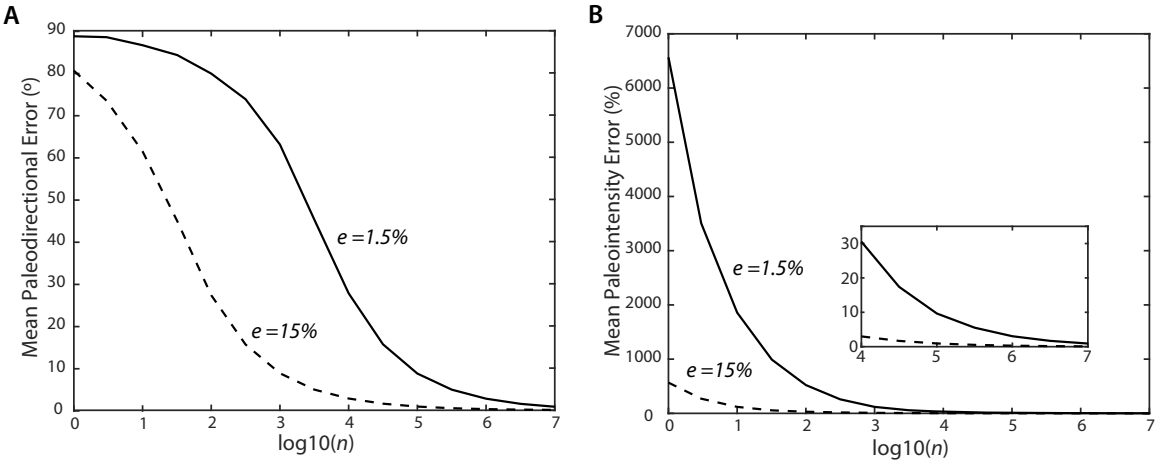

Figure 1. Paleodirectional and paleointensity errors associated with measuring the net moments of different numbers of single domain ferromagnetic grains with uniaxial easy axes distributed uniformly over the sphere. An underlying distribution of 10^8 grains was magnetized to an efficiency e of 1.5% or 15% in the paleofield direction (i.e., the net moment relative to the saturation remanence when all grains are magnetized in the same hemisphere centered around the paleofield direction $\hat{B}$). Then, n grains were chosen at random and their net moments computed and compared to that expected for $n \to \infty$. (a) Mean paleodirectional errors $\overline{\theta_e}$. (b) Mean paleointensity errors $\overline{m_e}$. Inset shows mean paleointensity errors for $n \geq 10^4$.

angular distribution of grain axes, $0 < e < 0.5$. We draw n grains at random from this population and calculate their resultant, $\vec{R}$, for n ranging from 1 to 10^8. We then compare the direction and magnitude of $\vec{R}(n)/n$ to that $\vec{R}(\infty)/\infty = e\hat{B}$ and compute the directional error:

$$\theta_e = \text{acos}\left[\hat{B} \cdot \vec{R}(n)/n\right] \tag{1}$$

and the paleointensity error:

$$m_e = 1 - \frac{\vec{R}(n)/n}{e}. \tag{2}$$

We then repeated each of these experiments for 10,000 trials to calculate the mean values $\overline{\theta_e}$ and $\overline{m_e}$. This number of trial repetitions was found to insure convergence of the final estimated values of $\overline{\theta_e}$ and $\overline{m_e}$ to better than 1% of the true means.

For $e \sim 0.015$ and 0.15, we find that $n_{\text{min}} = \sim$70,000 and 800 for $\overline{\theta_e} = 10°$ and ~25,000 and ~250 for $\overline{m_e} = 20\%$ (Figure 1). Therefore, these intuitively specified directional and intensity error limits yield very similar values of n_{min}. Given the single grain moment m above, these n_{min} values correspond to net moments of ~2 and 0.2×10^{-14} Am^2 for $\overline{\theta_e} = 10°$ and ~8 and 0.8×10^{-15} Am^2 for $\overline{m_e} = 20\%$. An analytical study using Langevin theory for detrital remanent magnetization carried by single domain magnetite grains by *Kirschvink* [1981] estimated a minimum net moment of 6×10^{-14} Am^2 for grains with radii about twice those considered here and for maximum mean directional errors of 5°. A recent analytical approach by *Berndt et al.* [2016] of magnetite grain assemblages found that paleointensity errors exceeded 20% and paleodirectional errors exceeded 20° for net moments of $\sim 10^{-15}$–10^{-14} Am^2. In summary, three very different independent analyses by this study, *Kirschvink* [1981] and *Berndt et al.* [2016] have found that natural samples should preserve paleomagnetically useful information down to natural remanent moments of 10^{-15}–10^{-14} Am^2, 100–1000 times below that measurable with standard superconducting rock magnetometers.

3. Description of Net Moment Technique

Having demonstrated the need for high-sensitivity moment magnetometry, we now describe our technique in detail. We focus on the computation of net magnetic moments from measurements of the magnetic field of geological samples whose external field is close to that of a magnetic dipole. Dipole moments are powerful ways to represent experimental data because (I) they are the elemental building blocks of magnetization distributions; (II) magnetic fields of distant sources behave as those of single magnetic dipoles; (III) the external magnetic field produced by specific source geometries can be very close or even identical to that of a magnetic

dipole [*Collinson*, 1983; *Jackson*, 1999; *Reitz et al*., 1979]. We assume that the samples are analyzed in a zero-field environment—for instance, inside a magnetically shielded room or container—such that no observable induced magnetization component is present and background remanent magnetization is near zero due to the use of low-moment sample holders. These simplifications make the moment magnetometry problem for magnetic microscopy far more tractable than magnetic surveys of crustal magnetization [e.g., *Parker*, 1991].

Regarding (I), magnetization is a vector quantity that is defined as the macroscopic average of dipole moments in a small volume element. Thus, magnetic dipoles are fundamentally connected to magnetization distributions, which are ultimately composed of individual electron magnetic moments. As for (II), the magnetic field of any source of finite size approaches asymptotically the field of a magnetic dipole as the distance between the source and the observer (e.g., magnetic sensor) increases. Expressing the external magnetic field of such a source as an expansion of spherical harmonics field terms shows that at large distances the dipole term prevails over higher order multipoles [*Jackson*, 1999]. Owing to the orthogonality of the spherical harmonics basis, none of the higher order terms affects the dipole moment (i.e., they all have zero magnetic dipole moment). Interestingly, the coefficient of the dipole term in the spherical harmonics expansion corresponds to the integral of the magnetization (net magnetic moment) [*Jackson*, 1999; *Stratton*, 2007]. Moreover, the dipole moment term is invariant with respect to the origin of the spherical harmonics expansion [*Epton and Dembart*, 1995; *Wikswo and Swinney*, 1985], which is particularly important for intricate magnetizations distributions for which the choice of a suitable origin for the expansion may not be obvious. Finally, (III) stems from the fact that certain symmetrical source configurations yield fields external to the magnetization distributions that are identical to (e.g., uniformly magnetized sphere) or very close to (e.g., uniformly magnetized cylinder with specific aspect ratio) the field of a magnetic dipole even at somewhat small distances.

Next, we show how the magnetic moment can be recovered from magnetic field measurements for different experimental configurations.

3.1. Recovering the Moment

The field of a magnetic dipole is given by

$$\vec{B}(\vec{r}) = \frac{\mu_0}{4\pi}\left\{\frac{3\vec{m}\cdot\left(\vec{r}-\vec{r'}\right)}{|\vec{r}-\vec{r'}|^5}\left(\vec{r}-\vec{r'}\right)-\frac{\vec{m}}{|\vec{r}-\vec{r'}|^3}\right\}, \tag{3}$$

where $\vec{m}$ is the magnetic moment, $\vec{r}$ and $\vec{r'}$ represent the positions of the sensor and of the dipole, respectively, and $\vec{B}$ is the magnetic field. In the absence of noise, we only need one set of measurements of the three components of the magnetic field of a dipolar source at a known distance [B_x (r), B_y (r), B_z (r)] to recover the net moment:

$$\vec{m} = \frac{4\pi}{\mu_0}|\vec{r}-\vec{r'}|^3\left\{\frac{3}{2}\frac{\vec{B}(\vec{r})\cdot\left(\vec{r}-\vec{r'}\right)}{|\vec{r}-\vec{r'}|^2}\left(\vec{r}-\vec{r'}\right)-\vec{B}(\vec{r})\right\}, \tag{4}$$

given that for known $\vec{r}-\vec{r'}$ the moment $\vec{m}$ is completely specified by $\vec{B}$. [The expression above can be easily obtained from (3) the after some manipulation making use of vector identities.]

Alternatively, instead of using a single measurement of the vector magnetic field, we can also recover the moment from three measurements of a single component of the field taken at suitable positions (e.g., the z-component of the magnetic field measured at three points on a horizontal plane above the source):

$$\begin{bmatrix} B_z(x_1,y_1,h) \\ B_z(x_2,y_2,h) \\ B_z(x_3,y_3,h) \end{bmatrix} = \frac{\mu_0}{4\pi}\begin{bmatrix} \frac{3x_1h}{(x_1^2+y_1^2+h^2)^{5/2}} & \frac{3y_1h}{(x_1^2+y_1^2+h^2)^{5/2}} & \frac{2h^2-x_1^2-y_1^2}{(x_1^2+y_1^2+h^2)^{5/2}} \\ \frac{3x_2h}{(x_2^2+y_2^2+h^2)^{5/2}} & \frac{3y_2h}{(x_2^2+y_2^2+h^2)^{5/2}} & \frac{2h^2-x_2^2-y_2^2}{(x_2^2+y_2^2+h^2)^{5/2}} \\ \frac{3x_3h}{(x_3^2+y_3^2+h^2)^{5/2}} & \frac{3y_3h}{(x_3^2+y_3^2+h^2)^{5/2}} & \frac{2h^2-x_3^2-y_3^2}{(x_3^2+y_3^2+h^2)^{5/2}} \end{bmatrix}\begin{bmatrix} m_x \\ m_y \\ m_z \end{bmatrix}, \tag{5}$$

where we assume that the dipole is located at the origin of the coordinate system (without loss of generality), and that the field is measured at three points on the plane $z=h$ parallel to the sample: (x_1, y_1, h),

(x_2, y_2, h), and (x_3, y_3, h). Such points must be chosen so as to yield a nonsingular, invertible matrix when solving the system of linear equations (5). This can be easily accomplished by avoiding (i) points where $B_z = 0$; (ii) three points that are greatly clustered; (iii) three points that lie on a line (e.g., $x = y$, $x = 0$, $y = 0$) or on the circle of radius $h\sqrt{2}$ centered about the origin.

Under real experimental conditions, sensor noise will degrade the vector magnetic field measurement $\vec{B}$ in (4) or the three measurements of the z-component of $\vec{B}$ in (5), thereby affecting the recovered moment by adding a spurious component. To ameliorate this problem, an average magnetic moment estimate can be computed using (4) for repeated measurements of $\vec{B}$ at the same distance from the source. In the single-component approach, we can combine a larger number of measurements to obtain an overdetermined system of linear equations whose approximate solution can be found via the method of least squares.

Whereas these two approaches are very straightforward due to the fact they are linear in the recovered three components of the moment, the accuracy in recovering the moment is directly related to how well known is the position of the sensor relative to the source. For this reason, such methods tend to perform better when the sensor-to-sample distance is large compared to the sample size, such that small uncertainties in the relative position do not noticeably impact accuracy (similarly, sensors with large sensing areas or volumes tend to minimize the influence of position uncertainty, owing to averaging effects).

In scanning magnetic microscopy, the magnetic sensor is typically brought as close as possible to the sample in order to maximize sensitivity and achieve superior spatial resolution. Errors in assessing the relative distance between the measurement positions and the sample location may not be negligible, particularly because the exact location of the equivalent dipole in a given geological sample is usually not known. Therefore, a different approach is required to accurately recover the net moment.

In essence, we generalize the least-squares method for solving the linear system (5) to account for the uncertainty in the dipole location. Specifically, we assume a dipole that is no longer located at the origin but at the coordinate $\vec{r'} = (x_0, y_0, 0)$ (we take the z-coordinate to be zero without loss of generality). Measurements of the field component normal to the sample, B_z, are again taken at a plane parallel to the x–y plane and distance h above it. We then have to find six parameters in total, three of which (spatial coordinates of the dipole) exhibit a nonlinear dependence with B_z. Thus, we have transformed our linear least-squares problem into a nonlinear one. Notice that B_z still preserves its linear dependence on the three remaining parameters (i.e., the components of the dipole moment) such that the least-squares problem is actually of mixed form or separable. We also consider that the magnetic field measurements are taken at positions on an evenly spaced rectangular grid.

We draw attention to the fact that using a single component of the magnetic field to determine the magnetic moment does not lead to loss of information or to a decrease in accuracy. Maxwell's equations establish that the magnetic field in a region devoid of sources (i.e., outside the sample, where we take measurements of the field) can be completely represented by the gradient of a scalar function satisfying Laplace's equation. This scalar potential means that all three field components are tightly interconnected and that a single component essentially carries all the information about the full vector field [*Lima and Weiss*, 2009]. This refutes recent unsubstantiated assertions that single-component maps do not provide unique vector field constraints [*Cottrell et al*., 2016; *Dare et al*., 2016]. Notice that these relationships hold for the magnetic field measured and computed *on surfaces* rather than in a pointwise manner. This fact has been recognized and exploited in geophysics since as early as 1945 [*Vestine and Davids*, 1945], and is extensively used in magnetic surveys from the local to the planetary scale [*Blakely*, 1996; *Purucker, 1990, 2008*].

In mathematical terms, we wish to find the parameter vector $\boldsymbol{p} = (x_0, y_0, h, m_x, m_y, m_z)^T = (\boldsymbol{x}, \boldsymbol{m})^T$, that minimizes the objective (cost) function defined as the residual sum of squares between the experimental magnetic field data and the dipole model field computed at the same locations (the symbol ^{T} denotes the transpose of a vector or matrix). That is to say:

$$\underset{\boldsymbol{x},\boldsymbol{m}\in\mathbb{R}^3}{\text{minimize}} \quad \|\boldsymbol{b_z} - \boldsymbol{G}(\boldsymbol{x})\boldsymbol{m}\|_2^2, \tag{6}$$

where $\boldsymbol{G}$ stands for the geometry matrix, $\boldsymbol{b_z}$ is the vector with the measurements of the z-component of the magnetic field on the planar grid, and $\|\cdot\|_2^2$ denotes the Euclidean norm (2-norm) squared.

We can use two different methods to solve (6). Case 1: a nonlinear optimization algorithm searches a six-dimensional parameter space for the optimal parameter vector $\boldsymbol{p}$ that minimizes the residuals. Case 2: we take advantage of the linear relationship between the magnetic field and the magnetic moment (i.e., the separability of the nonlinear least-squares problem [*Golub and Pereyra*, 2003]) to split the solution into linear and nonlinear parts. Here, a nonlinear optimization algorithm searches instead a reduced three-dimensional space corresponding to the $\boldsymbol{x}$ parameter vector. For each iteration of the optimization algorithm, a linear least-squares problem is solved to find the moment vector $\boldsymbol{m}(\boldsymbol{x})$ for the particular geometry matrix $\boldsymbol{G}(\boldsymbol{x})$:

$$\underset{\boldsymbol{x} \in \mathbb{R}^3}{\text{minimize}} \qquad ||\boldsymbol{b_z} - \boldsymbol{G}(\boldsymbol{x})\boldsymbol{m}(\boldsymbol{x})||_2^2, \tag{7}$$

$$\text{subject to } \boldsymbol{m}(\boldsymbol{x}) = \boldsymbol{G}^{+}(\boldsymbol{x})\,\boldsymbol{b_z}$$

where $\boldsymbol{G}^{+}(\boldsymbol{x}) = \left(\boldsymbol{G}(\boldsymbol{x})^T\boldsymbol{G}(\boldsymbol{x})\right)^{-1}\boldsymbol{G}(\boldsymbol{x})^T$ is the pseudoinverse of $\boldsymbol{G}(\boldsymbol{x})$. (That is to say, for each set of values for x, y, and h, chosen by the optimization algorithm we solve for $[m_x, m_y, m_z]$.)

One possible interpretation of this problem is recognizing that the components of the magnetic moment are the coefficients in a linear combination of scalar-valued functions $G_1(x,y,h)$, $G_2(x,y,h)$, and $G_3(x,y,h)$ that best approximates the field data:

$$b_z(x,y,h) = m_x G_1(x-x_0, y-y_0, h) + m_y G_2(x-x_0, y-y_0, h) + m_z G_3(x-x_0, y-y_0, h). \tag{8}$$

The advantage of the first approach is mostly shorter computational times (this is specific for the single-dipole case), with the tradeoff that the larger search space may lead to trapping at local minima and suboptimal solutions, particularly when the true source distribution cannot be exactly represented by a single dipole. On the other hand, the second approach yields solutions in a smaller number of iterations (although usually taking longer time) and is less prone to trapping at local minima.

In both cases, the optimization problem is solved multiple times using different initial guesses for the optimization parameters at each time that are obtained via random perturbations of the nominal values (with typical perturbations of 5–20% of initial guesses). The final error (residual) associated with each solution is compared and the one with the smallest error is chosen. This procedure helps ensure that local minima are avoided and that the solution that best approximates the experimental data is found. Usually, we compute the optimization problem 20–100 times, obtaining final solutions within 30–60 s on a moderately fast PC with a single Intel Quad Core i7-950 CPU and 12 GB of RAM, depending on size of the field map and how far the nominal initial guess is from the true solution. We typically use hundreds to thousands of data points to recover the three net moment components, resulting in a greatly overdetermined problem that increases the robustness of the solution in the presence of higher noise levels. Clearly, the larger the number of data points, the greater the time to complete each iteration of the optimization procedure. In general, noisy field data require using fine-sampled field maps with a larger number of data points in the optimization so as to achieve adequate accuracy in the moment estimates.

It is often advantageous to run the optimization algorithm a single time while observing the output of the model during the initial iterations, particularly prior to starting to processing maps associated with demagnetization or remagnetization sequences of a sample. This allows us to manually adjust the initial guess for the optimization parameters so that they are not very far off from the true configuration of the experiment, speeding up the overall optimization procedure and helping ensure convergence. For instance, good estimates for the horizontal coordinates (x_0, y_0) of the dipole can be directly obtained from the location with maximum field strength in the total field map computed from the measured normal field component map. Estimates for the distance between the measurement plane and the sources (also called liftoff distance or sensor-to-sample distance), h, can be obtained by measuring standard samples such as thin current-carrying wires and small magnetized dots, or even by optical measurements depending on the type of magnetometer used [*Baudenbacher et al*., 2002; *Hankard et al*., 2009; *Lima et al*., 2014].

When solving the six-parameter optimization problem (Case 1), estimates for the moment components can be more easily obtained in spherical coordinates—moment strength, inclination, and declination—and then converted back to rectangular coordinates. Inclination can be roughly estimated by visually comparing the greatest positive and negative values of the measured field $\boldsymbol{b_z}$. Approximately equal values are indicative of zero inclination, whereas predominantly positive or negative values correspond to $+90°$ or $-90°$,

respectively (or else to $-90°$ or $+90°$, respectively, depending on the convention used). Intermediate inclinations can be reasonably estimated from the ratio between the greatest positive and negative values. Declination can be estimated from the angle between the y axis and the line connecting the greatest positive and negative values of the field map. Lastly, an order-of-magnitude estimate of the strength can be found by comparing the overall magnitude of the field values in the experimental and model field maps.

We emphasize that only coarse estimates of the optimization parameters are required to achieve rapid convergence, and they are usually only necessary for the first step in a demagnetization or remagnetization sequence. In this case, it is also beneficial to use the solution of a particular sequence step as the initial guess for the subsequent step, as this can speed up the overall processing time. Henceforth we focus on the Case 1 algorithm, which was the approach chosen to process all the synthetic and experimental data shown in this paper.

3.2. Optimization Algorithm

To solve the optimization problem, we utilized a nonlinear least-squares algorithm with no added bound constraints based on the subspace trust-region method described in *Coleman and Li* [1994, 1996], which is implemented in MATLAB® by the function *lsqnonlin*. For the typical field strengths observed in scanning SQUID microscopy and field maps expressed in nano-tesla (nT) units, we used as stopping criteria (i) a tolerance for changes in the value of the objective function of 1×10^{-12}, (ii) a tolerance for changes in the size of a step of 1×10^{-14}, (iii) a maximum number of iterations of 3000, and (iv) a maximum number of function evaluations of 6000.

We also carried out a number of tests using the Nelder-Mead simplex algorithm [*Lagarias et al*., 1998], which is implemented in MATLAB by the function *fminsearch*. However, we did not find any appreciable increase in the accuracy of solutions that would warrant the longer convergence times associated with that algorithm.

3.3. Uniqueness

The question of uniqueness of the solution to the net moment inverse problem is intrinsically related to the existence of magnetically silent sources (annihilators) with nonzero moments. In order to uniquely recover the net moment from magnetic field measurements, there cannot exist any magnetization distribution with nonzero moment in a given class of magnetizations that produces no external magnetic field. Otherwise, two magnetizations with different net moments would be indistinguishable as they would produce the same observable field. Usually, a comprehensive characterization of silent sources in a general setting involves sophisticated mathematics [*Baratchart et al*., 2013; *Parker*, 1994], but this issue is greatly simplified in the case of a single dipolar source. In this situation, it is easy to see from (5) and its generalization for N measurement points that there does not exist a nonzero dipole that produces a zero field everywhere on the plane $z=h$. Thus, the solution to problem (6) is inherently unique provided that the field is adequately sampled on the plane, such that the discretization of the problem is not an issue.

3.4. Finite Sensor Size

Depending on the magnetic sensing technology used in the mapping of the sample's field, it may be necessary to take into account the integration of the field over the sensing area or sensing volume of the magnetic sensor. This is typically dictated by the ratio between sensor size and sensor-to-sample separation: the smaller the sensor size compared to the separation, the less important the integration effects are (i.e., they become essentially multiplication by a constant). Because magnetic fields vary slower in space as one moves away from the sources, they come to be more uniform over the integration area as the separation between sensor and sources increases, thus diminishing averaging effects over the sensing region. Interestingly, arbitrarily enlarging the sensing region for a given sensor-to-sensor distance aiming to improve sensitivity may actually have the opposite effect because magnetic fields of finite source distributions average to zero over large areas or volumes [*Weiss et al*., 2001]. Modeling magnetic sensors as spatial filters is a powerful tool to analyze the effects of integration over a sensing region [*Lima et al*., 2002; *Roth and Wikswo*, 1990]. In particular, for SQUID sensors, the optimum tradeoff for pointwise sources consists of having the sensor size roughly match the sensor-to-sample distance [*Fong et al*., 2005].

Whereas it is outside of the scope of this paper to discuss in detail magnetic sensor modeling, we point out that (5) can be easily modified to take into account the effects of a finite sensing region. In this case, the

left-hand side of (5) would no longer be the magnetic field measured at a set of points, but instead the field averaged over regions centered about those points. Gaussian quadrature formulas [*Abramowitz and Stegun*, 1965; *Kim and Song*, 1997] are particularly useful for incorporating averaging effects into the model as they maintain the overall structure of (5), which then becomes equivalent to a weighted sum of magnetic dipoles:

$$\begin{bmatrix} \overline{B_z}(x_1,y_1,h) \\ \overline{B_z}(x_2,y_2,h) \\ \overline{B_z}(x_3,y_3,h) \end{bmatrix} = \frac{\mu_0 C}{4\pi} \sum_{k=1}^{N} \left(w_k \begin{bmatrix} \frac{3x_{1,k}h}{\left(x_{1,k}^2+y_{1,k}^2+h^2\right)^{5/2}} & \frac{3y_{1,k}h}{\left(x_{1,k}^2+y_{1,k}^2+h^2\right)^{5/2}} & \frac{2h^2-x_{1,k}^2-y_{1,k}^2}{\left(x_{1,k}^2+y_{1,k}^2+h^2\right)^{5/2}} \\ \frac{3x_{2,k}h}{\left(x_{2,k}^2+y_{2,k}^2+h^2\right)^{5/2}} & \frac{3y_{2,k}h}{\left(x_{2,k}^2+y_{2,k}^2+h^2\right)^{5/2}} & \frac{2h^2-x_{2,k}^2-y_{2,k}^2}{\left(x_{2,k}^2+y_{2,k}^2+h^2\right)^{5/2}} \\ \frac{3x_{3,k}h}{\left(x_{3,k}^2+y_{3,k}^2+h^2\right)^{5/2}} & \frac{3y_{3,k}h}{\left(x_{3,k}^2+y_{3,k}^2+h^2\right)^{5/2}} & \frac{2h^2-x_{3,k}^2-y_{3,k}^2}{\left(x_{3,k}^2+y_{3,k}^2+h^2\right)^{5/2}} \end{bmatrix} \right) \begin{bmatrix} m_x \\ m_y \\ m_z \end{bmatrix}, \tag{9}$$

where $x_{i,k}=x_i+\Delta_{x,k}$, $y_{i,k}=y_i+\Delta_{y,k}$ (for $i=1, 2, 3$), and C, w_k, $\Delta_{x,k}$, $\Delta_{y,k}$ are given by the integration region and the chosen N-point quadrature formula, and the overbar denotes integration over a region (an area in this case). Alternatively, the sensor response could be deconvolved from the measured data prior to solving the optimization problem so as to undo the effects associated with sensor geometry [*Lima et al*., 2002]. The main disadvantage of incorporating sensing region modeling is the increase in processing time.

In our experimental setup, the averaging effects over the sensing area usually represent a second-order correction and can often be neglected in view of other sources of error. SQUID devices are calibrated by measuring their response to a known applied uniform field. Given that the effective size of the sensing area in our SQUID chips is between 50×50 and 80×80 μm^2 (depending on their exact design) and that the sensor-to-sample distance is typically greater than 100 μm (200 μm in this study, with an effective distance to the equivalent dipole for our three-dimensional samples greater than 300–400 μm), we can show that the mean field does not differ significantly from the field value at the center of the sensing area.

To illustrate this point, let us consider the z-component of the field of a magnetic dipole measured on a plane at a distance h above it. To simplify the calculations we assume that the dipole points in the $+z$ direction, so as to produce an axisymmetrical field, and is located at the origin:

$$B_z(x,y,h)=\frac{\mu_0 m_z}{4\pi}\frac{2h^2-x^2-y^2}{(x^2+y^2+h^2)^{5/2}}=C_0\frac{2h^2-\rho^2}{(\rho^2+h^2)^{5/2}}, \tag{10}$$

where $\rho=\sqrt{x^2+y^2}$ and $C_0=\frac{\mu_0 m_z}{4\pi}$. For a SQUID sensor with effective area $A_{eff}=\pi a^2$ placed at the location (x_0,y_0,h), the output signal is proportional to the magnetic flux Φ through A_{eff}:

$$\Phi(x_0,y_0,h)=\int_{-a}^{a}\int_{-\sqrt{a^2-y^2}}^{\sqrt{a^2-y^2}} B_z(x-x_0,y-y_0,h)\,dx\,dy, \tag{11}$$

where we assume a circular sensing area to simplify the calculations.

We wish to determine what the error is in approximating the integral in (11) by $\tilde{\Phi}(x_0,y_0,h)=A_{eff}B_z(x_0,y_0,h)$ (i.e., by size of the integration area times the field evaluated at the center of the integration area). In principle, such an approximation is reasonable: given that B_z is continuous for $h \neq 0$, the mean value theorem for double integrals [*Marsden and Tromba*, 2012] ensures that there is a point $(\tilde{x},\tilde{y})$ within the integration region such that $\Phi(x_0,y_0,h)=A_{eff}B_z(\tilde{x},\tilde{y},h)$; however, that point may or may not be the center (x_0,y_0), which is what may lead to inaccuracies in the approximation. The largest error in the approximation occurs when the sensor is exactly above the test dipole, where B_z is maximum and the field values at all points in the integration region are less than or equal to the one at the central point. In this situation, the actual flux measured by the sensor is given by

$$\Phi(0,0,h)=\int_0^{2\pi}\int_0^{a} C_0\frac{2h^2-\rho^2}{(\rho^2+h^2)^{5/2}}\rho\,d\rho\,d\varphi=\frac{2\pi C_0 a^2}{(a^2+h^2)^{3/2}}, \tag{12}$$

in which we express the double integral in cylindrical coordinates for convenience. The approximate flux (i.e., assuming a fixed calibration factor for the sensor) is

$$\tilde{\Phi}(0,0,h)=\frac{2\pi a^2 C_0}{h^3}. \tag{13}$$

Computing the relative error between the two fluxes yields

$$E_{max}=\frac{(a^2+h^2)^{3/2}}{h^3}-1=\frac{(\gamma^2+1)^{3/2}}{\gamma^3}-1, \tag{14}$$

for $h=\gamma a$. Substituting $\gamma=8$ in (14), which is a typical value for γ in our setup, we get that the maximum relative pointwise error is about 2.4%. Notice that this overestimate is the *maximum* error in our approximation at a single point and that the discrepancy is much smaller (or even zero) in other regions of the field map (e.g., where the field exhibit a bilinear behavior). Thus, the overall impact on the net moment estimate is further reduced by the least-squares optimization procedure. Similarly, the shape of the actual sensing area (a square) and its lack of axial symmetry can be neglected in our case, as they affect the estimate even less. Hence, in the analysis that follows averaging effects were not included in our computations. However, such corrections may be important when using other magnetic field sensing technologies and experimental setups.

4. Synthetic Samples and Sensitivity Analysis

As in our approach, standard rock magnetometers infer magnetic moment by assuming the measured samples are dipolar or nearly dipolar. The development of these magnetometers was guided by modeling the magnetic fields of samples of various sizes and shapes, with the sizes and placement of their coils optimized such that the inferred moments achieved accuracy to a few % for cm-scale uniformly magnetized cylindrical and cubic samples [*Collinson*, 1983]. Following this approach, here we determine the maximum size of uniformly magnetized samples whose moments can be accurately retrieved using our technique given the typical sensor-sample distance of $\sim$100 μm encountered in SQUID microscopy. Specifically, we tested our moment estimation technique with synthetic magnetic field maps obtained using three different types of sources — single magnetic dipole, uniformly magnetized square measuring 50 $\times$ 50 μm^2, and uniformly magnetized cube of 50 $\times$ 50 $\times$ 50 μm^3 — and various combinations of noise level and sensor-to-sample distance. Gaussian white noise was added to field maps to simulate measurements under actual experimental conditions. For the noisy cases, we generated 15 field maps for each source type-noise level combination. This enabled us to determine the statistical dispersion in the recovered parameters due to different realizations of the noise stochastic process.

As the sensor-to-sample distance was varied, the step size (i.e., discretization) and the mapping area were adjusted accordingly so as to obtain field maps with identical number of points and comparable field decay at the edges. In this way, we ensured that possible artifacts due to inconsistent discretization and cropping of the magnetic field data were avoided. All synthetic field maps were composed of 64 $\times$ 64 points with a mapping area-discretization configuration similar to the one shown in the central image in Figure 2c. For dipolar test sources, the grid spacing and mapping area varied from 0.79 to 39.7 μm and from 50 $\times$ 50 to 2500 $\times$ 2500 μm^2, respectively, as the sensor-to-sample distance varied from 10 to 500 μm. For the uniformly magnetized square source and the same range of sensor-to-sample distances, grid spacing and mapping area varied from 2.94 to 47.7 μm and from 185 $\times$ 185 to 3000 $\times$ 3000 μm^2, respectively. In the case of the uniformly magnetized cube, grid spacing and mapping area varied from 3.90 to 50.0 μm and from 246 $\times$ 246 to 3200 $\times$ 3200 μm^2, respectively, for the same range of sensor-to-sample distances.

Regarding the test sources chosen, the magnetic dipole allows us to assess how sensitive the algorithm is to the initial guesses for the model parameters and to noise, because the same source is used in the forward and inverse problems. By using the uniformly magnetized square and cube test sources, we can then determine how performance is degraded as the source strays from a purely dipolar behavior and how noise

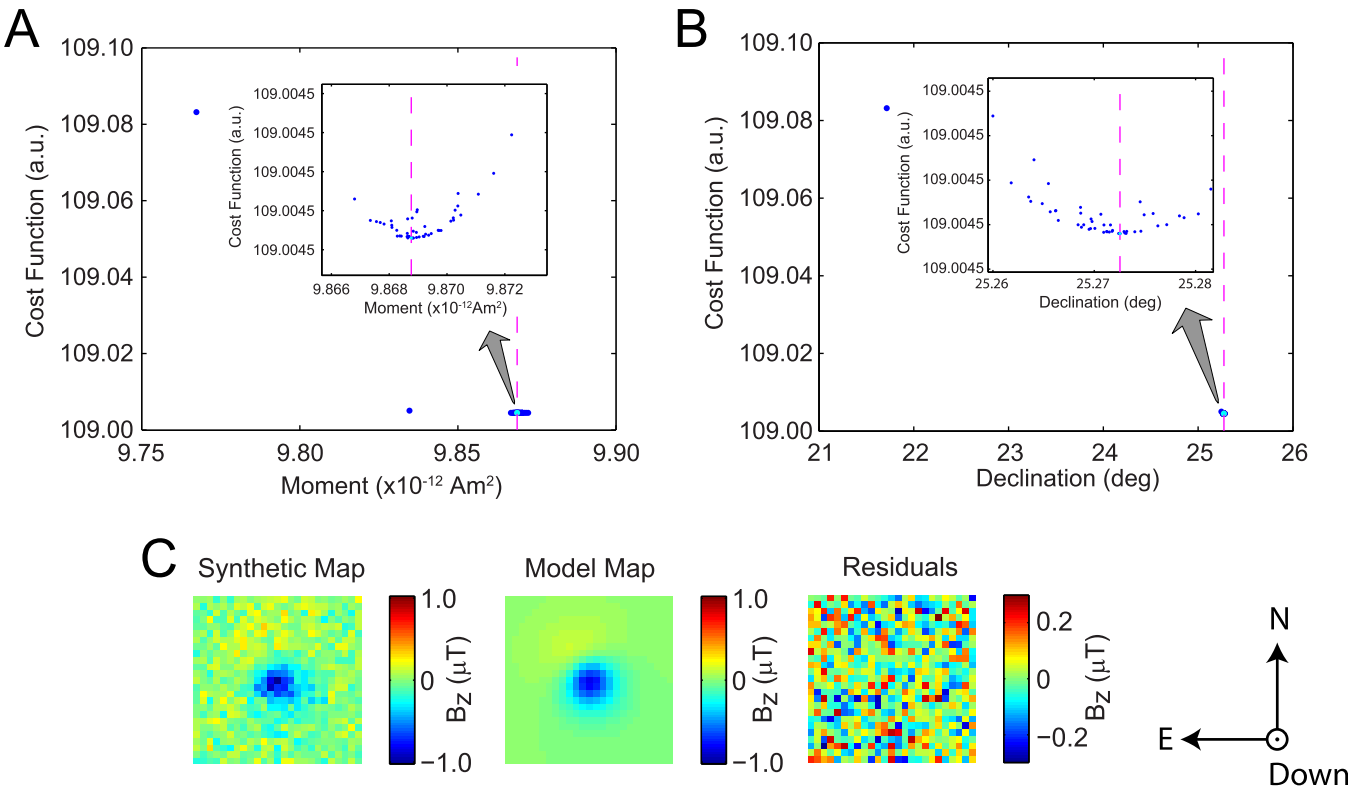

Figure 2. Optimization procedure for estimating the net moment of the source. The optimization problem was solved 50 times, each with different initial guesses for the model parameters. The solution with the smallest cost function value (i.e., smallest residual) was then selected as the estimated magnetic moment. (Cost is displayed in arbitrary units – a.u.) Here, to highlight the dispersion in the solutions, we show an unfavorable case in which a nondipolar test source is mapped at a small sensor-to-sample distance and field measurements are corrupted by high levels of noise, negatively impacting the accuracy of the estimated moment (see section 4 for detailed discussion). (a) Plot of the recovered moment magnitude for each of the 50 calculated solutions with their corresponding costs. Each dark blue dot represents a single solution. Inset shows detail of the region containing solutions with the smallest costs. Axis labels with the same value indicate that final errors in the solutions differ by less than 10^{-5} a.u., which reflects the fact that the main source of mismatch between synthetic and model field maps is the noise component. Dashed magenta line and corresponding light blue dot indicate the best solution to the optimization problem. (b) Plot of the recovered declination for each of the 50 calculated solutions with their corresponding costs. Other model parameters exhibit analogous behavior. (c) (left) synthetic field map of a uniformly magnetized 50 × 50 × 50 μm^3 cube measured on a 64 × 64 planar grid 100 μm above it with 12.1 μm grid spacing. White noise was added to yield an extremely poor SNR of 0 dB (i.e., a 1:1 proportion of noise and signal). The magnetic moment of the cube is 1.0×10^{-11} Am^2 at −45° inclination and 20° declination. (middle) field map of the magnetic dipole that best fits the data, which was found using the abovementioned optimization procedure. (right) difference between synthetic and model maps, showing that they differ essentially by the noise component.

further impacts the magnetic moment estimates. In this case, the sensor-to-sample distance intrinsically controls the proportion of higher order multipole terms (e.g., quadrupole, octupole, etc.) introduced in the forward model relative to the dipolar term. Whereas all these higher order terms have zero net moment by virtue of the orthogonality properties of spherical harmonics, they may still negatively affect the net moment estimates: given that those estimates are based on the matching of experimental and model field maps, the dipole model parameters will be tuned so as to best match the whole experimental map and not just the dipole component present in it. Therefore, care should be taken to ensure that the dipole term is indeed dominant in the experimental data. If necessary, the magnetic field map should be upward continued to decrease the contribution of higher order terms. The prevalence of the dipole term can usually be evaluated by analyzing the residual map and observing how correlated features eventually present in it change as liftoff distance varies. Notice that this upward continuation approach often yields better results than measuring the sample from a greater distance, as higher signal-to-noise ratio (SNR) can be achieved and contamination of the field map by background sources and adjacent impurities is minimized.

Like in any technique that recovers magnetic moments from measurements of the magnetic field, the SNR determines the weakest magnetic moment that can be recovered (i.e., magnetic moment sensitivity). The SNR, in turn, is a function of the sensor-to-sample distance: the closer the sensor is to the sample, the stronger the magnetic field (and, hence, the SNR) but the less likely the source distribution behaves as a single dipole. Getting too close to the sources may also exacerbate the integration effects associated with the finite size of magnetic sensors.

For a given field map, the optimization was solved 50 times, each one with initial parameter estimates that consisted of random perturbations of the initial guess by as much as 10% (up to $\pm 4°$ and $\pm 8°$ for the inclination and declination parameters, respectively). As explained in section 3, the net moment estimate was obtained by analyzing those 50 solutions to the optimization problem and picking the one with the smallest residual (Figure 2). For each combination of source type and SNR, we repeated this procedure for 15 field maps yielding a total of 15 net moment estimates: in the noiseless case, we used identical field maps, whereas in the noisy cases, we used maps with different realizations of the random noise. We then computed the mean net moment by (vector) averaging the 15 net moment estimates. We also calculated the sample standard deviation and sample mean (or median depending on the case) for the moment magnitude, recovered height, and angular error.

Notice that the noiseless maps allow us to demonstrate the consistency of the net moment estimates, given that no scatter should be observed in such estimates when repeatedly inverting identical data if the global minimum of the objective function is being effectively reached during the optimization procedure.

We begin by analyzing the noiseless case for all three synthetic sources (Figures 3a, 4a, and 5a). As expected, the scatter in the recovered quantities — denoted by error bars representing plus or minus one sample standard deviation — is negligible when no noise is present. Notice that the standard error of the mean (SEM), which measures the standard deviation of the error in the sample mean relative to the true mean, can be obtained by scaling the sample standard deviation by $1/\sqrt{N}$, where N is the sample size. In our case, this corresponds to shrinking the error bars by a factor of $\approx$3.9 to represent the SEM. Owing to the skewed nature of the distribution of angular error in the net moment estimates, we display the median and first and third quartiles in that case.

There is no dependence of estimated moment magnitude and direction on liftoff distance for the dipole, as expected (Figures 3a and 4a). There is also no deviation in recovered liftoff with respect to the true liftoff distance (Figure 5a). However, there is noticeable dependence of those quantities for the uniformly magnetized square and cube sources. Such dependence is stronger for the square, which should be expected given that the center of the cube lies deeper than that of the square (by definition, the liftoff distance is measured between the magnetic sensor and the top of the source distribution/sample). In particular, the recovered dipole lies deeper than the actual test source to compensate for the slower spatial decay of the magnetic field in those cases. As a consequence, the magnitude of the moment has to increase so as to match the strength of the magnetic field. The resulting error in the estimated moment, especially in the magnitude, can be quite large ($>$250%) when the liftoff distance is smaller than the source dimensions (i.e., $<$ 50 μm for square plate). For larger liftoffs ($>$ 100 μm), the dipole term becomes dominant and accuracy improves rapidly.

Introducing noise in the field maps results in scatter in the net moment estimates and in other model parameters. At moderate noise levels (20 dB SNR or 10:1 proportion between signal and noise), a small scatter of a few percent is noticeable in the moment magnitude (Figure 3b) and of about a degree in the direction (Figure 4b). The scatter in the recovered liftoff is comparatively smaller and barely noticeable (Figure 5b). Increasing the noise level to yield an SNR of 10 dB (i.e., 3.2:1 proportion of signal and noise) has the effect of increasing the scatter by a comparable amount (Figures 3c, 4c, and 5c). Finally, for a very poor SNR of 0 dB (i.e., equal proportion of signal and noise) the scatter increases further by another factor of $\approx$3. Notice that in all noisy cases, the overall trend of the recovered quantities observed in the noiseless case for the three sources is preserved.

An important point that can be seen in Figures 3–5 is that the mean net moment typically yields better estimates of the true moment's magnitude and direction than directly computing the mean or median of the individual parameters. For example, the angular error of the mean net moment is noticeably smaller than the median of the angular errors of the individual solutions. Whereas in paleomagnetic studies it may not be practical to repeatedly map a sample 15 times (for each magnetization/demagnetization step), as was done in this computational experiment, it is nevertheless beneficial to make a few repeated maps so as to improve the accuracy of the net moment estimates through vector averaging, particularly when measuring very weak samples with degraded signal-to-noise ratios.

5. Application to Geological Samples

To experimentally validate our technique, we imparted controlled magnetizations on geological samples with approximately dipolar magnetizations. We measured the samples using both a commercial SQUID

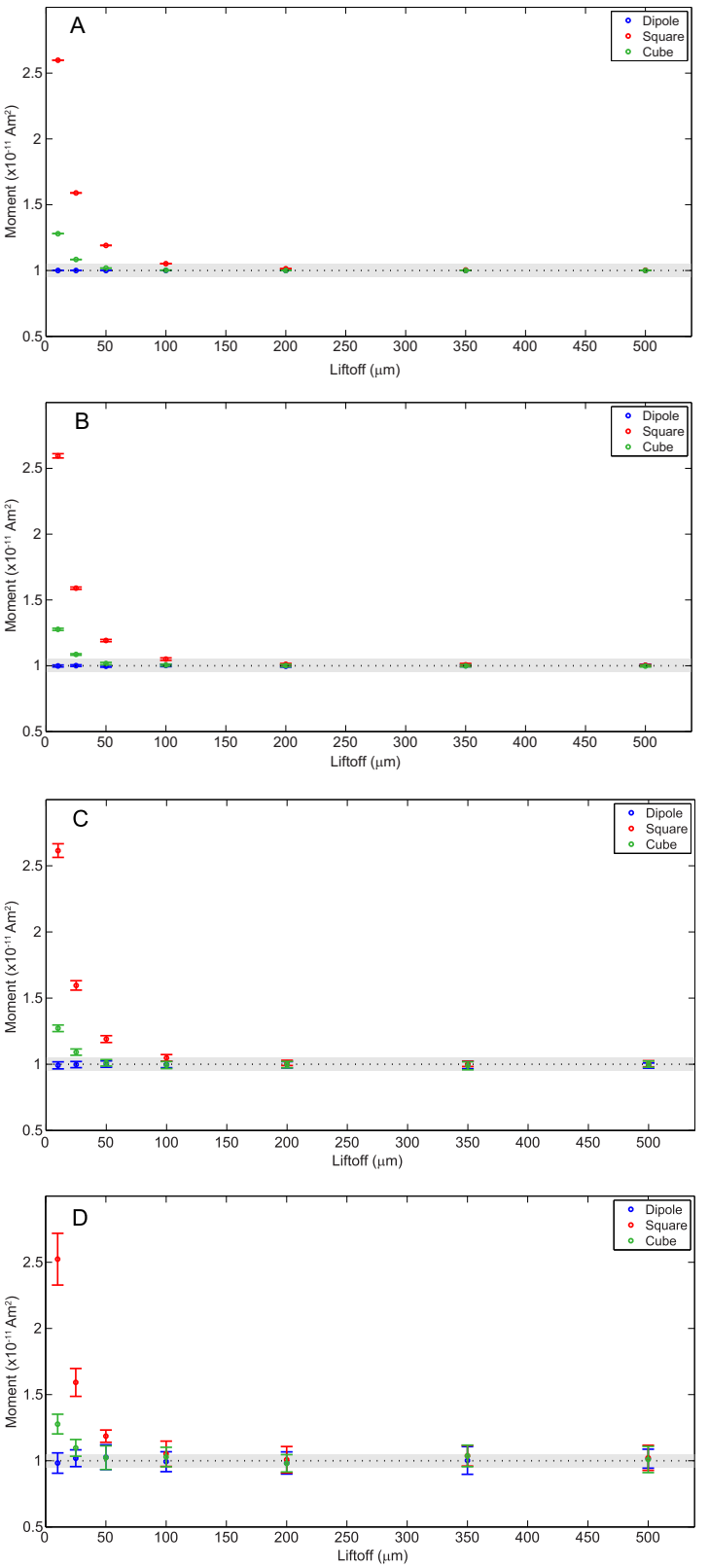

Figure 3. Magnitude of estimated net moments as a function of liftoff distance for all three test sources and different noise levels. Each colored circle represents the magnitude of the mean net moment (the mean of the magnitudes of estimated moments was omitted for clarity purposes, as it virtually coincides with the magnitude of the mean net moment). The error bars represent plus or minus one sample standard deviation. (a) Noiseless case (SNR = ∞). (b) 10:1 proportion of signal and noise (SNR = 20 dB). (c) 3:1 proportion of signal and noise (SNR = 10 dB). (d) 1:1 proportion of signal and noise (SNR = 0 dB). Black dashed line indicates the true magnitude of the moment, and the gray rectangle denotes the region in the plot where deviations from the true magnitude are smaller than or equal to 5%. By definition, the liftoff distance is measured between the magnetic sensor and the top of the source distribution/sample.

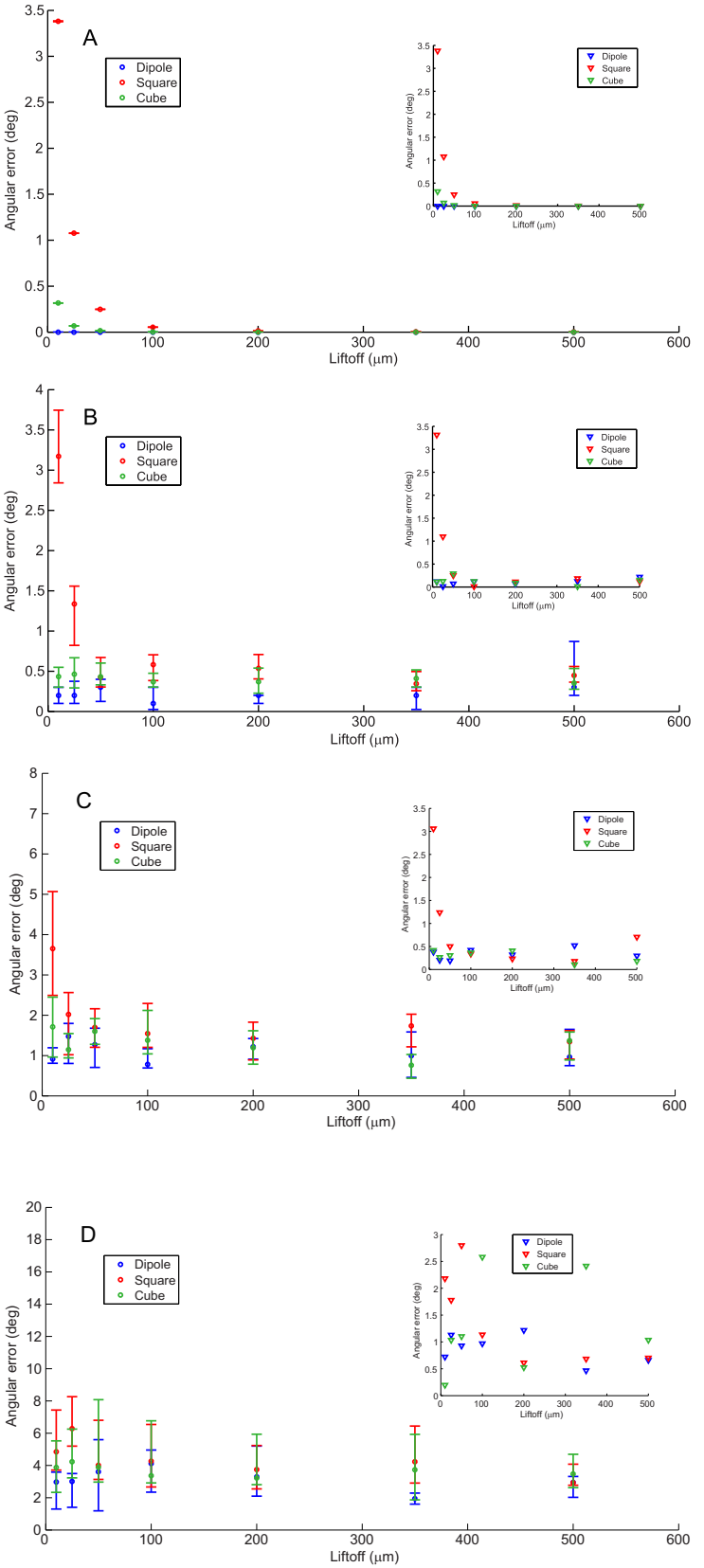

Figure 4. Error in the direction of the estimated net moments as a function of liftoff distance for all three test sources and different noise levels. Each colored circle represents the sample median of the angular error. The error bars denote the first and third sample quartiles. Colored triangles in the insets show the angular error of the mean net moment, which is typically smaller than the sample median. (a) Noiseless case (SNR = ∞). (b) 10:1 proportion of signal and noise (SNR = 20 dB). (c) 3:1 proportion of signal and noise (SNR = 10 dB). (d) 1:1 proportion of signal and noise (SNR = 0 dB).

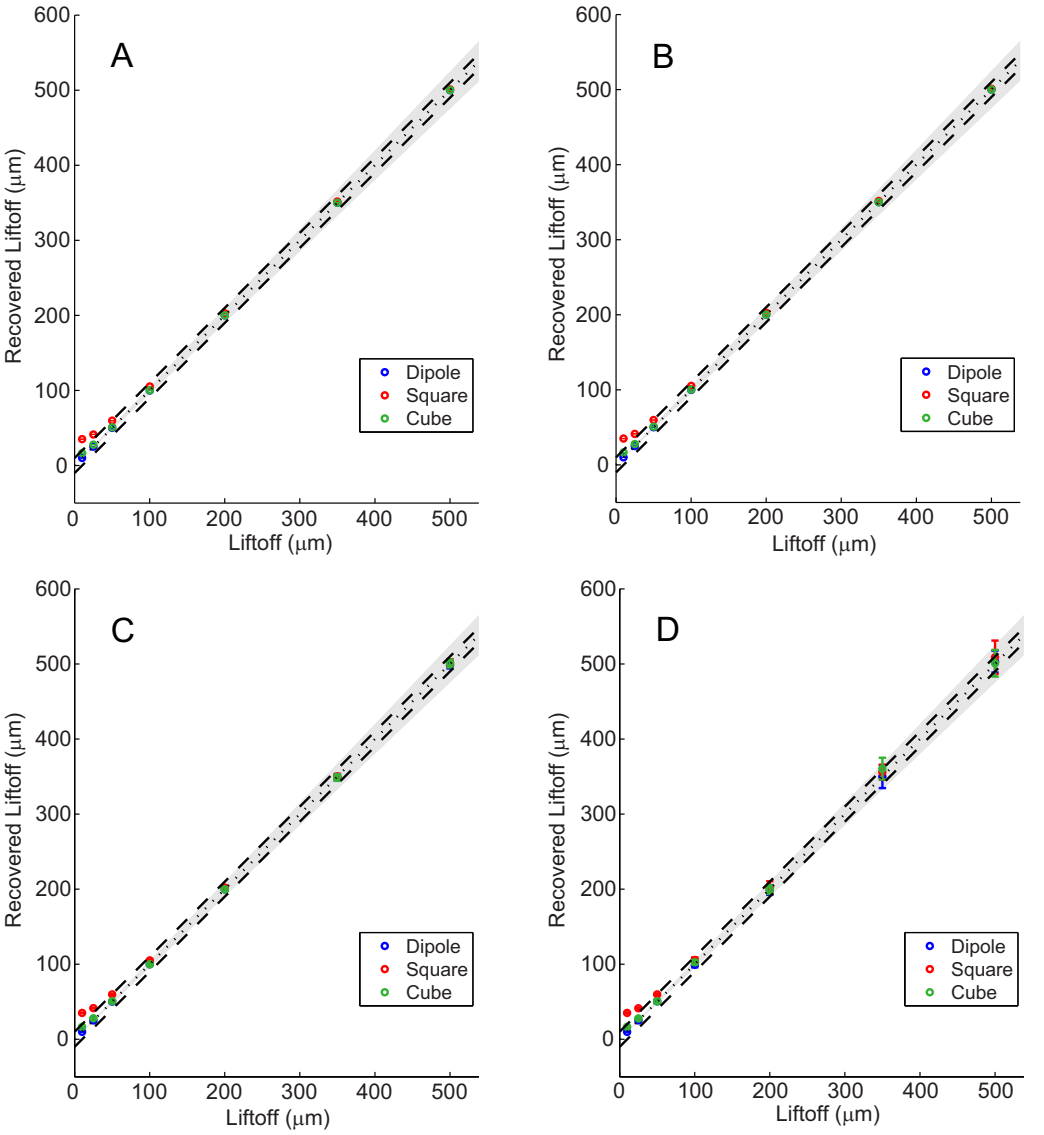

Figure 5. Recovered liftoff as a function of liftoff distance for all three test sources and different noise levels. Each colored circle represents the recovered liftoff. The error bars represent plus or minus one sample standard deviation. (a) Noiseless case (SNR = ∞). (b) 10:1 proportion of signal and noise (SNR = 20 dB). (c) 3:1 proportion of signal and noise (SNR = 10 dB). (d) 1:1 proportion of signal and noise (SNR = 0 dB). Black dotted line indicates the true liftoff, and the gray area denotes the region in the plot where deviations from the true liftoff are smaller than or equal to 5%. Two black dashed lines represent ± 10 μm deviation from the true liftoff.

rock magnetometer (2G Enterprises 755 SRM) (sensitivity 1×10^{-12} Am^2) [*Fuller et al.*, 1985] and the SQUID microscope (sensitivity 1×10^{-15} Am^2) [*Fong et al.*, 2005] housed in the MIT Paleomagnetism Laboratory. For each demagnetization step, the samples were successively measured on both instruments and transported between shielded rooms in a magnetically shielded can. We estimate the reproducibility in repositioning the samples in each instrument to be better than 2–3°, with the declination being the main source of uncertainty. Note that although recent studies of 2G pass-through SRMs have observed systematic angular errors of a few degrees in the orientation of the measurement axes and a small discrepancy in sensitivity owing to imperfections in the manufacturing and characterization of the instrument [*Jackson et al.*, 2010; *Oda and Xuan*, 2014; *Oda et al.*, 2016], we independently calibrated the SQUID axis orientations for our system after its arrival at MIT (also our system is equipped with high-homogeneity coils).

In this section, no vector averaging of moment estimates obtained from SM data was performed, so as to provide a fair and direct comparison between our technique and standard SQUID rock magnetometry. Note

however that each data point measured with our 2G system actually consists of a vector average of four moment measurements obtained by rotating the sample about the *z* (up-down) axis in 90° intervals. (An exception is section 5.3, which is not part of the comparison, where a few AF demagnetization steps in the sequence were repeated and SM moment data were averaged.)

5.1. Impact Spherule From Lonar Crater, India

We began by magnetizing a ~300 μm impact melt spherule from Lonar crater in India [*Weiss et al*., 2010] by imparting a 200 mT isothermal remanent magnetization (IRM). Following the IRM application but prior to measuring it with the 2G SRM, the sample was then mounted on a magnetically clean acid-washed 2.5 cm diameter quartz disc using cyanoacrylate (superglue) in order to minimize the contribution to the net moment from the quartz disc. The 2G SRM measured a moment of 5.8×10^{-9} Am^2, >1000× above its moment resolution. The remounting on a magnetically clean disc ensured that the moment of the quartz disc is weak compared to the sample moment measured with the 2G SRM but has the limitation that the original sample orientation was lost due to difficulties in maintaining the absolute orientation of such a small sample between the IRM application and gluing it on the disc. The loss of orientation is not a major issue since having a magnetization that is not purely vertically oriented is beneficial for testing the technique more generally. Note that *Weiss et al*. [2010] observed that Lonar spherules have no appreciable anisotropy of remanence.

This sample was then progressively alternating-field (AF) demagnetized. For each demagnetization step, the sample was measured on both instruments and the results compared (Figures 6a and 6b). The sample's moment decreased down to a minimum value of 4.0×10^{-11} Am^2, always remaining above the sensitivity limits of both magnetometers. This high moment explains why the measurements of the two magnetometers agree well for most of the demagnetization sequence. Although measurements from both instruments agree in general to within better than 10% in intensity and 4° in direction, there are discrepancies in direction and intensity for the final two demagnetization steps (160 and 200 mT) even though the sample moments at these steps according to the 2G SRM are still 2.6×10^{-11} and 5.1×10^{-11} Am^2, respectively (1.4×10^{-10} and 4.0×10^{-11}Am^2, respectively, according to SQUID microscope). In this AF range, the directional data from the SQUID microscope measurements show a ~60° change in declination with almost no change in inclination between the first (i.e., IRM) and last (AF 200 mT) steps. In contrast, the 2G data imply a hemisphere change and inclination shallowing in the last demagnetization step.

To determine which instrument is yielding more accurate data, we look at the SQUID microscope field maps of the first (Figure 6c) and last (Figure 6d) steps in the sequence. It is very clear that there is no visually perceptible change in inclination whereas declination varies by approximately 60°. Note that information about declination can be obtained from the line connecting the maximum and minimum fields in a map; inclination is associated with the ratio between the maximum and minimum fields in a map, with zero inclination corresponding to a ratio of 1. This suggests that, in this measurement scenario, the SQUID microscope data are much more accurate than the 2G data.

The reason for the superior performance of the SQUID microscope can be observed from Figure 6d: areas with weaker magnetization surround the spherule, likely from impurities in the quartz disc and dust particles that became trapped in the glue. The mapping area shown is 4×4 mm^2 and only reveals a small fraction of the contaminating magnetization that could be present in a 2.5 cm diameter quartz disc. The small discrepancy in Figure 6b in the beginning of the demagnetization sequence is likely attributed to contaminating magnetization, which is visible in the field maps, but the sources of uncertainty discussed in the beginning of aection 5 may also contribute in part to the observed differences. Such secondary sources have very little effect on the net moment estimates obtained from the SQUID microscopy data but directly affect the 2G measurements. This is an enormous advantage of magnetic microscopy over standard rock magnetometry when dealing with very weak samples: contamination in the sample holder is visually evident and its effects can be minimized in the vast majority of cases. On the other hand, it can be difficult to ascertain whether standard SQUID rock magnetometry data are partially biased or even dominated by secondary sources when measuring very weak samples. We emphasize that the observed discrepancies occur well above the detection limit of our 2G SRM (~1×10^{-12} Am^2), which underscores the necessity of utilizing ultra-clean mounting and handling techniques when analyzing very weakly magnetized samples. Such techniques minimize the amount of quartz and glue used to affix the sample and ensure that dust particles

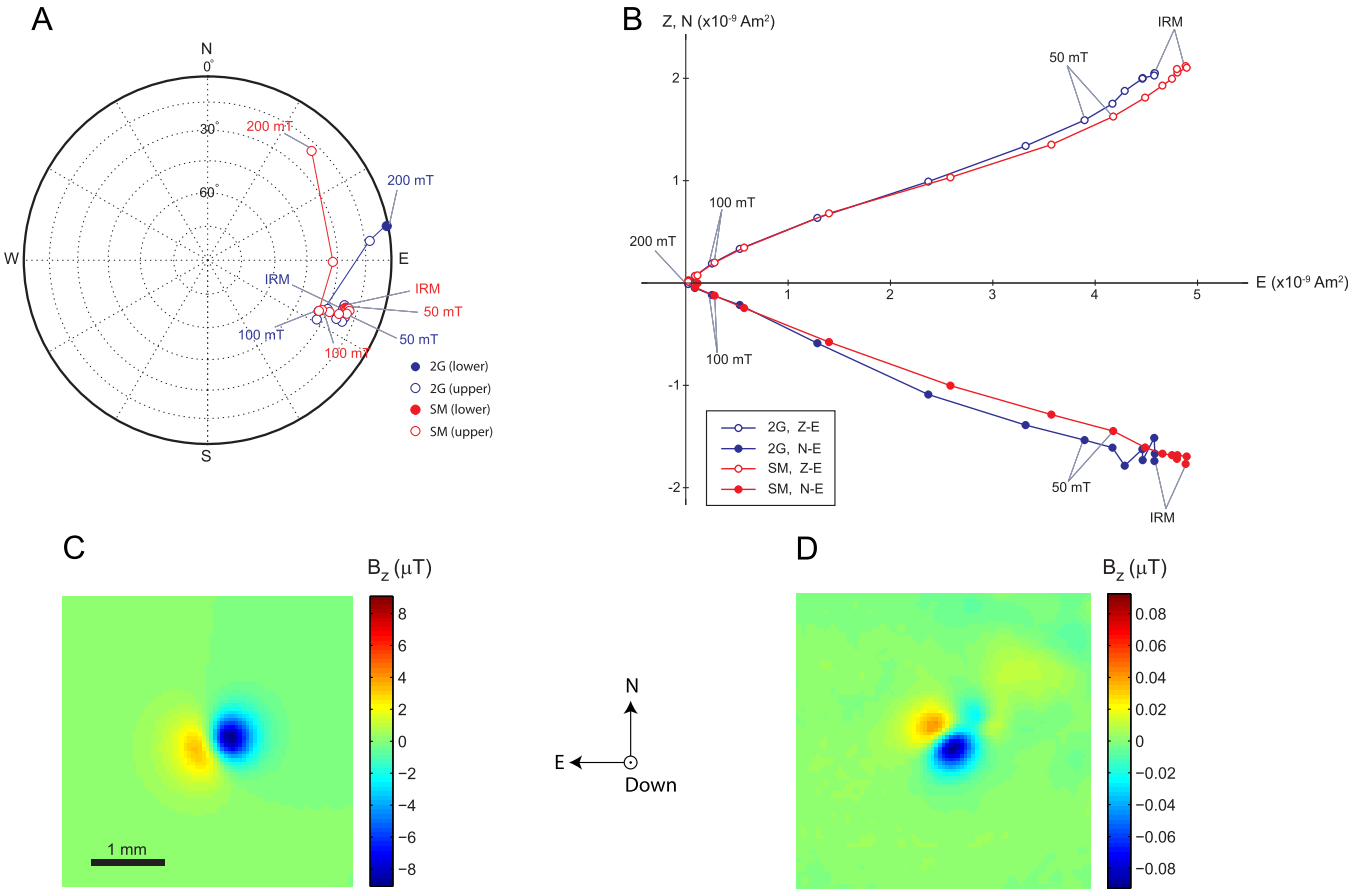

Figure 6. AF demagnetization of an impact melt spherule from Lonar crater in India. We imparted a 200 mT IRM to the spherule prior to mounting it on a quartz disc and subsequently carrying out the AF demagnetization steps. At each step, the spherule was measured on the 2G SRM and on our SQUID microscope (SM). (a) Net moment directional data shown on an equal area stereoplot (SQUID microscope data shown in red, 2G data shown in blue). Open symbols and solid lines represent projections on upper hemisphere and closed symbols and dashed lines represent projections on lower hemisphere. (b) Up-east (Z-E) and north-east (N-E) projections of the endpoints of the net moment vector shown (SQUID microscope data shown in red, 2G data shown in blue). (c) Vertical component (i.e., normal to the sample mount) of the sample's magnetic field after an IRM was imparted using a field of 0.2 T. (d) Vertical component of the sample's field after the final AF demagnetization step (200 mT peak field). Notice the ~60° change in declination between the two steps with almost no change in inclination. The magnetic field maps were measured ~200 μm above the sample on a 100 × 100 grid with 50 μm spacing.

do not stick to the specimen during preparation and subsequent AF or thermal demagnetization. For example, by mounting samples on >10 cm long, 3 mm diameter clean quartz rods instead of the 2.5 cm discs used here, *Fu et al*. [2012b] were able to measure and demagnetize the NRM of samples of the eucrite ALHA81001 down to below 5×10^{-12} Am^2.

5.2. Millbillillie Eucrite

Following our analysis of the Lonar spherule, we proceeded to measure a weaker sample: cutting dust from the Millbillillie eucrite [*Fu et al*., 2012a]. A clump of this material was mounted on a 2.5 cm diameter quartz disc using silver paste designed for scanning electron microscopy applications as a nonmagnetic adhesive. A TRM was imparted by heating the sample to 580°C while applying a 50 μT dc magnetic field, followed by thermal demagnetization steps up to 450°C (Figure 7). After imparting the TRM, the sample was dismounted and reglued on a clean nonmagnetic quartz disc to again reduce the effects of background sources on the 2G SRM measurements. As a result, the orientation of the applied field relative to the measured sample is unknown. During the course of thermal demagnetization, the sample's moment dropped below the noise limit of the 2G SRM (from a starting moment of 1.9×10^{-11} Am^2 down to 6.6×10^{-13}Am^2). Consequently, the 2G SRM data are noisier than the SQUID microscope data and do not trend to the origin, which we attribute to a combination of contamination sources and instrument noise. (We note again that the 2G data could have been improved somewhat if we had used thin quartz rod mounts instead of the 2.5 cm quartz discs used here.) In contrast to the 2G SRM data, the SQUID microscope data, which are less sensitive to

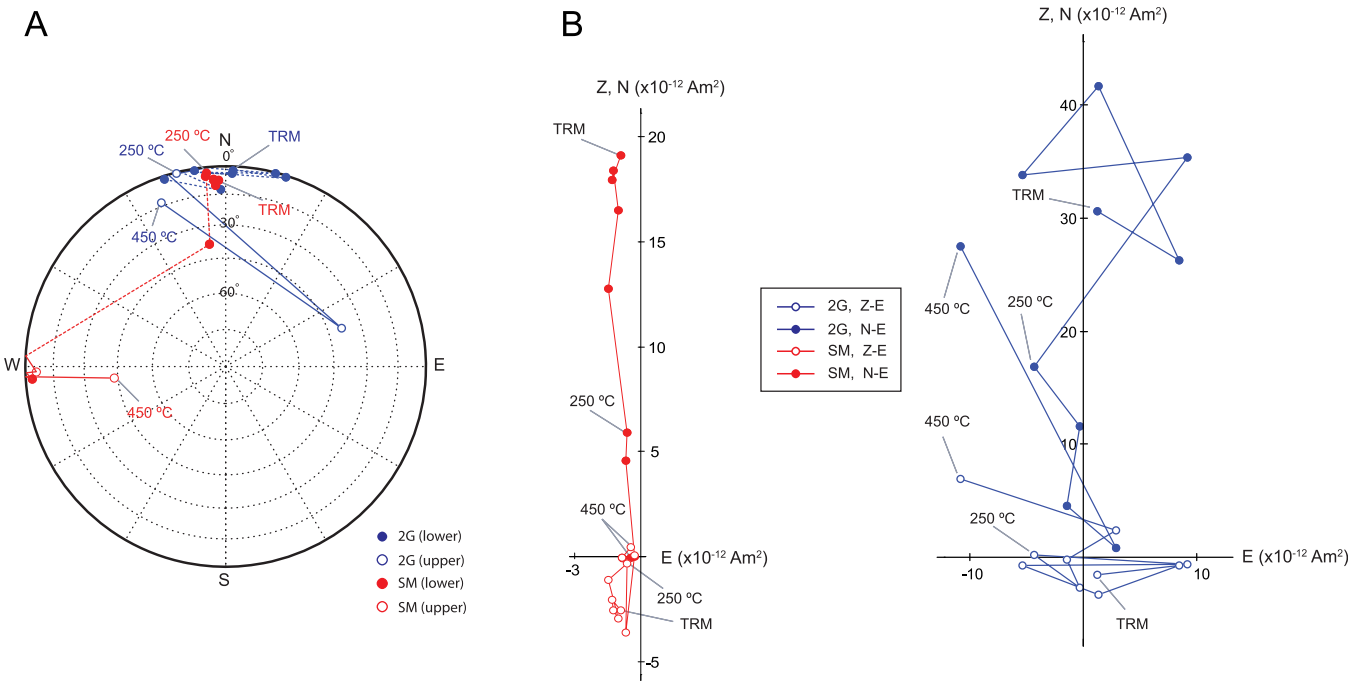

Figure 7. Thermal demagnetization of a small clump of cutting dust from the Millbillillie eucrite. We imparted a 50 μT TRM at 580°C to the sample prior to carrying out a sequence of thermal demagnetization steps. At each step, the sample was measured on the 2G SRM and on our SQUID microscope (SM). (a) Net moment directional data shown on an equal area stereoplot (SQUID microscope data shown in red, 2G data shown in blue). Open symbols and solid lines represent projections on upper hemisphere and closed symbols and dashed lines represent projections on lower hemisphere. (b) Up-east (Z-E) and north-east (N-E) projections of the endpoints of the net moment vector shown (SQUID microscope data shown in red, 2G data shown in blue). The magnetic field was mapped ~200 μm above the sample on a 100 × 100 grid with 40 μm spacing.

contamination on the sample mount and have better sensor resolution, are much cleaner and clearly trend to the origin up to temperatures of 450°C. Because this experiment only involved thermal demagnetization, it demonstrates that the observed discrepancies and scatter in the data cannot be attributed to spurious anhysteretic remanent magnetization (ARM) noise during AF demagnetization.

5.3. Detrital Zircons From the Jack Hills, Western Australia

Having established that the technique agrees with independent measurements for stronger samples and that it yields robust data for weaker samples, we proceeded to apply the technique to ultra-weak samples that cannot be detected using standard rock magnetometers. Detrital zircon crystals from the Jack Hills in Western Australia are an important target as they may preserve records of the origin and earliest evolution of the geodynamo [*Weiss et al*., 2015]. Their magnetizations typically fall below the detection limit of commercial rock magnetometers and often exhibit dipolar characteristics at the spatial scale of SQUID microscopy.

To demonstrate the performance of our ultra-high sensitivity moment magnetometry technique, we conducted AF demagnetization data on two detrital zircons from the Jack Hills (Figures 8 and 9) extracted from the Hadean zircon sampling site at Erawandoo Hill (site EHJH5 of *Weiss et al*. [2016, 2015]). Given their very weak moments, the two zircons were carefully mounted (together with two additional zircons) on an acid-washed 2.5 cm diameter quartz disc using cyanoacrylate. This procedure was performed in a clean room using nonmagnetic ceramic tools and an adjustable-volume pipette to minimize any chance of contamination by dust and other spurious sources of magnetic field. Three weakly magnetized markers (toner dots printed on paper) were initially glued near the edge of the disc for registration purposes and later removed once the location of each zircon in the NRM field map was unequivocally established. The first zircon clearly shows an origin-trending pattern with good directional stability (Figure 8), starting with an NRM moment of 6.0×10^{-14} Am^2 that demagnetized to 3.0×10^{-15}Am^2 by the AF 65 mT step. Moderate scatter in the data is predominantly due to the zircon's behavior under AF demagnetization and cannot be attributed to instrument noise. A few steps in the demagnetization sequence were repeated and moment data averaged to reduce this effect. This point is confirmed by the demagnetization of a second zircon, which exhibits larger

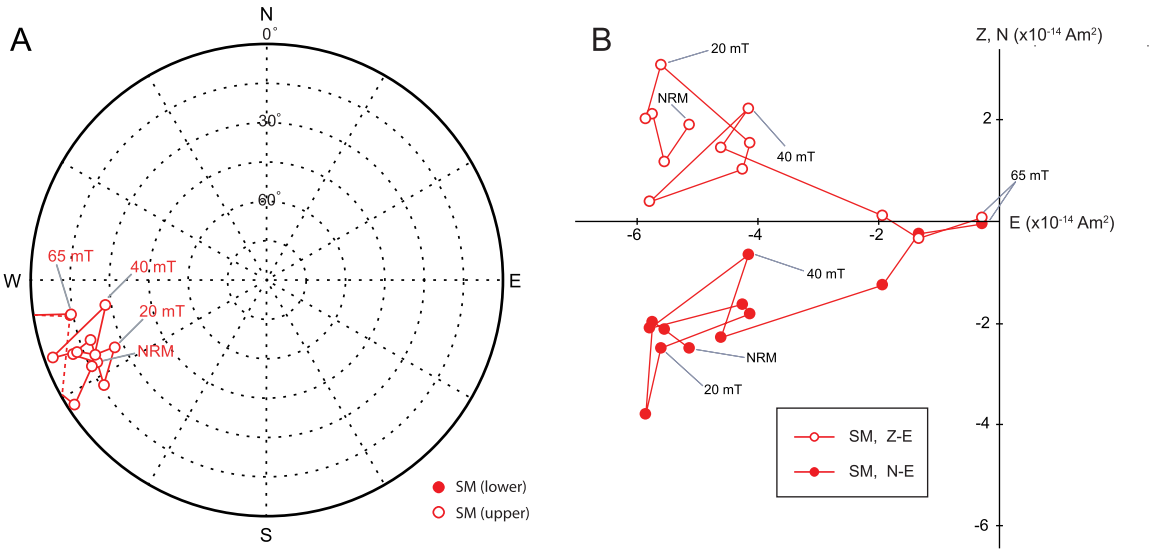

Figure 8. AF demagnetization sequence of a Jack Hills zircon measured with our SQUID microscope (SM). (a) Net moment directional data shown on an equal area stereoplot. Open symbols and solid lines represent projections on upper hemisphere and closed symbols and dashed lines represent projections on lower hemisphere. (b) Up-east (Z-E) and north-east (N-E) projections of the endpoints of the net moment vector. The magnetic field was mapped ~200 μm above the sample on a 121 × 121 grid with 25 μm spacing.

scatter and no decay despite having slightly stronger moment magnitudes (~1×10^{-13} Am^2) during most of the demagnetization sequence (Figure 9). It is clear that the observed differences in demagnetization pattern indeed stem from the samples. The relatively noisy demagnetization is likely due at least in part to the very small quantities of ferromagnetic material present in them (see section 2).

5.4. Other Ultra-Weak Magnetic Sources

To further test the detection limit of the SQUID microscope technique, we measured an ultra-weak secondary source present in a blob of silver paste on a quartz disc. SQUID microscope maps indicate its net moment is just 3.6×10^{-15} Am^2 (Figure 10), which is nearly the same moment magnitude as the last

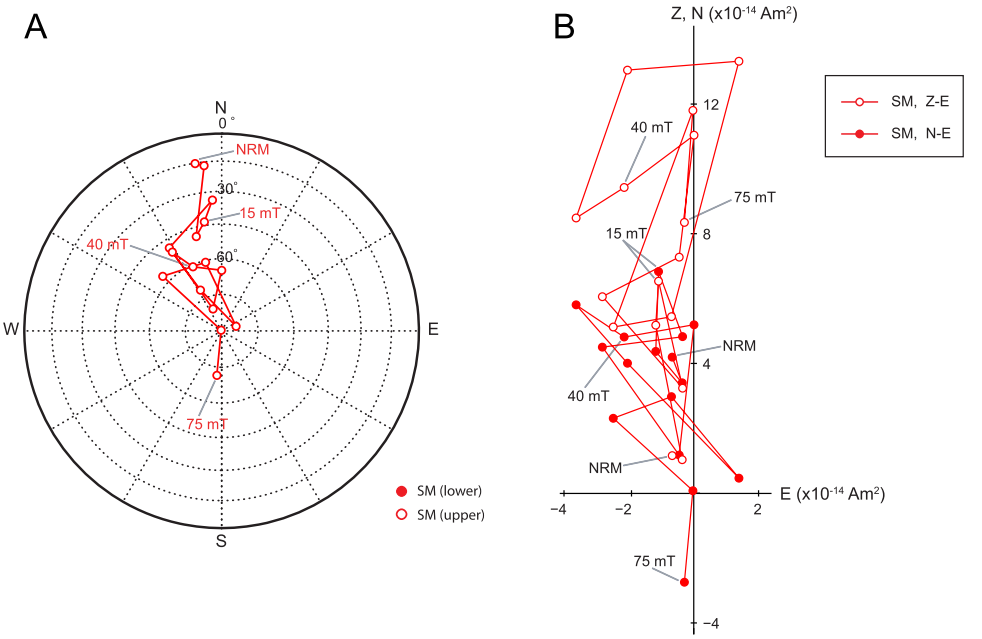

Figure 9. AF demagnetization sequence of a Jack Hills zircon measured with our SQUID microscope (SM). (a) Net moment directional data shown on an equal area stereoplot. (b) Up-east (Z-E) and north-east (N-E) projections of the endpoints of the net moment vector shown. The magnetic field was mapped ~200 μm above the sample on a 121 × 121 grid with 25 μm spacing.

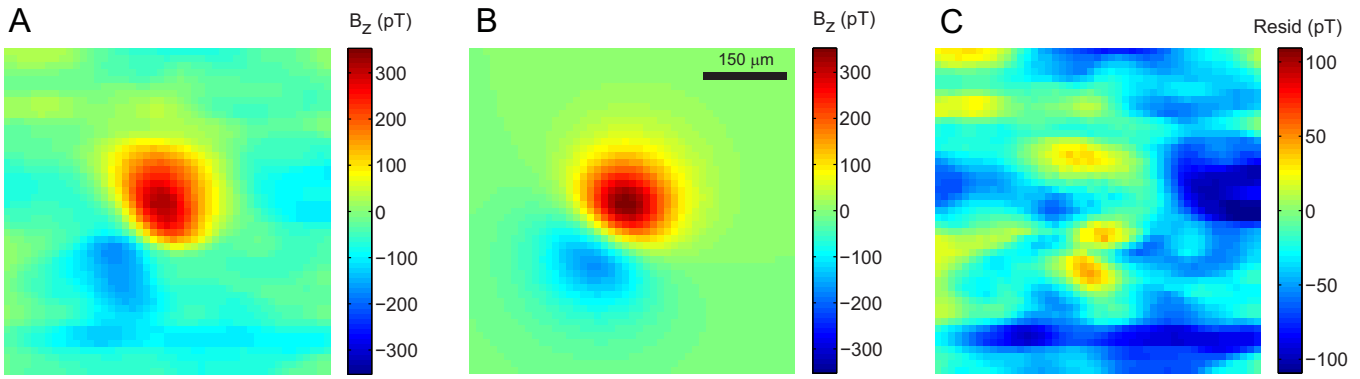

Figure 10. Detection and magnetic moment estimation of an ultra-weak magnetic moment consisting of a contaminating pointwise dipolar source present in a blob of silver paste. (a) Vertical component (i.e., normal to the sample mount) of the sample's magnetic field. (b) Field map of the magnetic dipole that best fits the data. (c) Difference between experimental and model maps, showing that they differ by very faint background sources that are still above the instrument noise. The magnetic moment of this source is 3.6×10^{-15} Am^2. The magnetic field was mapped ~200 μm above the sample on a 47 × 47 grid with 12.5 μm spacing.

demagnetization step of the first zircon (Figure 8). Despite being extremely faint, analysis of the residuals map reveals that we are still above the instrument's noise floor (typically in the few tens of pT, excluding long-term sensor output drift) by at least a factor of 5. This suggests that our actual detection limit — without additional signal processing to filter out instrument noise from the field maps — is in the mid to upper 10^{-16} Am^2 range. This encompasses the full range of sample moments expected to yield accurate paleodirectional and paleointensity constraints on the ancient field (section 2).

6. Conclusions

We have demonstrated that natural geologic samples should contain paleomagnetically useful information down to moments 100–1000 times below that detectable with standard rock magnetometers. To measure such samples, we developed an ultra-high sensitivity moment magnetometry technique based on magnetic microscopy that allows us to uniquely measure the net moments of extremely faint magnetic sources below 1×10^{-15} Am^2, thereby encompassing the full range of samples expected to be useful for paleomagnetism. We validated the technique by choosing suitable samples that could be independently measured with a commercial superconducting rock magnetometer. This comparison demonstrates some of the relative strengths of our technique relative to standard rock magnetometry, which not only include superior moment sensitivity but perhaps equally importantly a powerful ability to detect contaminating sources while minimizing their effect on the recovered moment. Our analysis with synthetic data revealed that the technique is accurate for dipolar sources even when measurements are contaminated with high levels of noise. We also showed that the major source of error in the net moment estimates is the possible deviation of the sample's magnetization from a magnetic dipole, an issue which also limits the accuracy of standard rock magnetometry. This can be ameliorated by upward continuing the magnetic field data so as to reduce the contribution of higher order multipole terms and enhance the contribution of the dipole term. Alternatively, more sophisticated source models could potentially be used to improve accuracy (e.g., multiple dipoles, incorporation of quadrupole terms into the modeling, uniformly magnetized areas/volumes) but at the expense of slowing down the algorithm. Although here we applied the technique to data only from SQUID microscopy, our technique can be directly applied to field maps obtained with other scanning magnetic microscopes and magnetic imaging techniques (e.g., magneto-optical imaging [*Uehara et al.*, 2010] and quantum diamond magnetometry [*Hong et al.*, 2013]).

Acknowledgments
The authors would like to thank the National Science Foundation grants DMS-1521765 and DMS-0934689 for partial support and Thomas F. Peterson, Jr. for his generous gift to the MIT Paleomagnetism Laboratory that also supported in part this research. The authors also thank Hirokuni Oda and an anonymous reviewer for helpful comments. Data sets and MATLAB® code used in this work are available as supporting information.

References

Abramowitz, M., and I. A. Stegun (1965), *Handbook of Mathematical Functions with Formulas, Graphs, and Mathematical Tables*, 1046 pp., Dover, N. Y.

Baratchart, L., D. P. Hardin, E. A. Lima, E. B. Saff, and B. P. Weiss (2013), Characterizing kernels of operators related to thin plate magnetizations via generalizations of Hodge decompositions, *Inverse Probl.*, *29*, 015004, doi:10.1088/0266-5611/29/1/015004.

Baudenbacher, F. J., N. T. Peters, and J. P. Wikswo (2002), High resolution low-temperature superconductivity superconducting quantum interference device microscope for imaging magnetic fields of samples at room temperatures, *Rev. Sci. Instrum.*, *73*, 1247–1254.

Berndt, T., A. R. Muxworthy, and K. Fabian (2016), Does size matter? Statistical limits of paleomagnetic field reconstruction from small rock specimens, *J. Geophys. Res. Solid Earth*, *121*, 15–26, doi:10.1002/2015JB012441

Blakely, R. J. (1996), *Potential Theory in Gravity and Magnetic Applications*, 441 pp., Cambridge Univ. Press, N. Y.

Butler, R. F., and S. K. Banerjee (1975), Theoretical single-domain size range in magnetite and titanomagnetite, *J. Geophys. Res.*, *80*, 4049–4058.

Coleman, T. F., and Y. Y. Li (1994), On the convergence of interior-reflective Newton methods for nonlinear minimization subject to bounds, *Math. Program.*, *67*, 189–224.

Coleman, T. F., and Y. Y. Li (1996), An interior trust region approach for nonlinear minimization subject to bounds, *SIAM J. Optim.*, *6*, 418–445, doi:10.1137/0806023.

Collinson, D. W. (1983), *Methods in Rock Magnetism and Paleomagnetism*, 503 pp., Chapman and Hall, N. Y.

Cottrell, R. D., J. A. Tarduno, R. K. Bono, M. S. Dare, and G. Mitra (2016), The inverse microconglomerate test: Further evidence for the preservation of Hadean magnetizations in metasediments of the Jack Hills, Western Australia, *Geophys. Res. Lett.*, *43*, 4215–4220, doi:10.1002/2016GL068150.

Dang, H. B., A. C. Maloof, and M. V. Romalis (2010), Ultrahigh sensitivity magnetic field and magnetization measurements with an atomic magnetometer, *Appl. Phys. Lett.*, *97*, 151110, doi:10.1063/1.3491215.

Dare, M. S., J. A. Tarduno, R. K. Bono, R. D. Cottrell, J. S. Beard, and K. P. Kodama (2016), Detrital magnetite and chromite in Jack Hills quartzite cobbles: Further evidence for the preservation of primary magnetizations and new insights into sediment provenance, *Earth Planet. Sci. Lett.*, *451*, 298–314, doi:10.1016/j.epsl.2016.05.009.

Epton, M. A., and B. Dembart (1995), Multipole translation theory for the 3-dimensional Laplace and Helmholtz equations, *SIAM J. Sci. Comput.*, *16*, 865–897, doi:10.1137/0916051.

Fong, L. E., J. R. Holzer, K. K. McBride, E. A. Lima, and F. Baudenbacher (2005), High resolution room-temperature sample scanning superconducting interference device microscope configurable for geological and biomagnetic applications, *Rev. Sci. Instrum.*, *76*, 053703.

Fu, R. R., B. P. Weiss, L. Li, C. Suavet, J. Gattacceca, and E. A. Lima (2012a), Magnetic fields on 4 Vesta as recorded in two eucrites, in *Lunar Planet Sci. Conf. XLIII*, abstract #1946.

Fu, R. R., B. P. Weiss, D. L. Shuster, J. Gattacceca, T. L. Grove, C. Suavet, E. A. Lima, L. Li, and A. T. Kuan (2012b), An ancient core dynamo in asteroid Vesta, *Science*, *338*, 238–241

Fu, R. R., et al. (2014), Solar nebula magnetic fields recorded in the Semarkona meteorite, *Science*, *346*, 1089–1092.

Fuller, M., W. S. Goree, and W. L. Goodman (1985), An introduction to the use of SQUID magnetometers in biomagnetism, in *Magnetite Biomineralization and Magnetoreception in Organisms: A New Biomagnetism*, edited by J. L. Kirschvink, D. S. Jones and B. J. MacFadden, pp. 103–151, Plenum, N. Y.

Gattacceca, J., M. Boustie, B. P. Weiss, P. Rochette, E. A. Lima, L. E. Fong, and F. J. Baudenbacher (2006), Investigating impact demagnetization through laser impacts and SQUID microscopy, *Geology*, *34*, 333–336.

Golub, G., and V. Pereyra (2003), Separable nonlinear least squares: The variable projection method and its applications, *Inverse Probl.*, *19*, R1–R26, doi:10.1088/0266-5611/19/2/201.

Hankard, F., J. Gattacceca, C. Fermon, M. Pannetier-Lecoeur, B. Langlais, Y. Quesnel, P. Rochette, and S. A. McEnroe (2009), Magnetic field microscopy of rock samples using a giant magnetoresistance-based scanning magnetometer, *Geochem. Geophys. Geosyst.*, *10*, Q10Y06, doi:10.1029/2009GC002750.

Hong, S., M. S. Grinolds, L. M. Pham, D. Le Sage, L. Luan, R. L. Walsworth, and A. Yacoby (2013), Nanoscale magnetometry with NV centers in diamond, *MRS Bull.*, *38*, 155–161, doi:10.1557/mrs.2013.23.

Jackson, J. D. (1999), *Classical Electrodynamics*, 3rd ed., 832 pp., John Wiley, N. Y.

Jackson, M., J. A. Bowles, I. Lascu, and P. Solheid (2010), Deconvolution of U-channel magnetometer data: Experimental study of accuracy, resolution, and stability of different inversion methods, *Geochem. Geophys. Geosyst.*, *11*, Q07Y10, doi:10.1029/2009GC002991.

Kim, K. J., and M. S. Song (1997), Symmetric quadrature formulas over a unit disk, Korean J. Comput. Appl. Math., 4, 179–192.

Kirschvink, J. L. (1981), How sensitive should a rock magnetometer be for use in paleomagnetism?, in *SQUID Applications to Geophysics*, edited by H. Weinstock and W. C. Overton, pp. 111–114, Soc. Explor. Geophys., Tulsa, Okla.

Kirschvink, J. L., Y. Isozaki, H. Shibuya, Y. Otofuji, T. D. Raub, I. A. Hilburn, T. Kasuya, M. Yokoyama, and M. Bonifacie (2015), Challenging the sensitivity limits of Paleomagnetism: Magnetostratigraphy of weakly magnetized Guadalupian–Lopingian (Permian) Limestone from Kyushu, Japan, Palaeogeogr. Palaeoclimatol. Palaeoecol., 284, 11–21.

Lagarias, J. C., J. A. Reeds, M. H. Wright, and P. E. Wright (1998), Convergence properties of the Nelder-Mead simplex method in low dimensions, *SIAM J. Optim.*, *9*, 112–147, doi:10.1137/s1052623496303470.

Lappe, S.-C. L. L., N. S. Church, T. Kasama, A. Bastos da Silva Fanta, G. Bromiley, R. E. Dunin-Borkowski, J. M. Feinberg, S. Russell, and R. J. Harrison (2011), Mineral magnetism of dusty olivine: A credible recorder of preaccretionary remanence, *Geochem. Geophys. Geosyst.*, *12*, Q12Z35, doi:10.1029/2011GC003811.

Lappe, S.-C. L. L., J. M. Feinberg, A. R. Muxworthy, and R. J. Harrison (2013), Comparison and calibration of nonheating paleointensity methods: A case study using dusty olivine, *Geochem. Geophys. Geosyst.*, *14*, 2143–2158, doi:10.1002/ggge.20141.

Lima, E. A., and B. P. Weiss (2009), Obtaining vector magnetic field maps from single-component measurements of geological samples, *J. Geophys. Res.*, *114*, B06102, doi:10.1029/2008JB006006.

Lima, E. A., A. C. Bruno, and J. Szczupak (2002), Two-dimensional deconvolution technique to recover the original magnetic field from the flux measured by SQUID planar gradiometers, *Superconductor Sci. Technol.*, *15*, 1259–1267, doi:10.1088/0953-2048/15/8/316.

Lima, E. A., A. Irimia, and J. P. Wikswo (2006), The magnetic inverse problem, in *The SQUID Handbook*, edited by J. Clarke and A. I. Braginski, pp. 139–267, Wiley-VCH, Weinheim, Germany.

Lima, E. A., B. P. Weiss, L. Baratchart, D. P. Hardin, and E. B. Saff (2013), Fast inversion of magnetic fields maps of unidirectional planar geological magnetization, *J. Geophys. Res. Solid Earth*, *118*, 2723–2752, doi:10.1002/jgrb.50229.

Lima, E. A., A. C. Bruno, H. R. Carvalho, and B. P. Weiss (2014), Scanning magnetic tunnel junction microscope for high-resolution imaging of remanent magnetization fields, *Meas. Sci. Technol.*, *25*, 105401, doi:10.1088/0957-0233/25/10/105401.

Marsden, J. E., and A. Tromba (2012), *Vector Calculus*, 6th ed., 545 pp., W. H. Freeman, N. Y.

Oda, H., and C. Xuan (2014), Deconvolution of continuous paleomagnetic data from pass-through magnetometer: A new algorithm to restore geomagnetic and environmental information based on realistic optimization, *Geochem. Geophys. Geosyst.*, *15*, 3907–3924, doi:10.1002/2014GC005513.

Oda, H., A. Usui, I. Miyagi, M. Joshima, B. P. Weiss, C. Schantz, L. E. Fong, K. K. McBride, R. Harder, and F. J. Baudenbacher (2011), Ultra-fine scale magnetostratigraphy of marine ferromanganese crust with the SQUID microscope, *Geology*, *39*, 227–230.

Oda, H., C. Xuan, and Y. Yamamoto (2016), Toward robust deconvolution of pass-through paleomagnetic measurements: New tool to estimate magnetometer sensor response and laser interferometry of sample positioning accuracy, *Earth Planets Space*, *68*, 109, doi: 10.1186/s40623-016-0493-2.

Parker, R. L. (1991), A theory of ideal bodies for seamount magnetism, *J. Geophys. Res.*, *96*, 16,101–16,112.

Parker, R. L. (1994), *Geophysical Inverse Theory*, 386 pp., Princeton Univ. Press, Princeton, N. J.

Purucker, M. E. (1990), The computation of vector magnetic anomalies: A comparison of techniques and errors, *Phys. Earth Planet. Inter.*, *62*, 231–245.

Purucker, M. E. (2008), A global model of the internal magnetic field of the Moon based on Lunar Prospector magnetometer observations, *Icarus*, *197*, 19–23.

Reitz, J. R., F. J. Milford, and R. W. Christy (1979), *Foundations of Electromagnetic Theory*, 3rd ed., 544 pp., Addison-Wesley, Reading, Mass.

Roth, B. J., and J. P. Wikswo (1990), Apodized pickup coils for improved spatial resolution of SQUID magnetometers, *Rev. Sci. Instrum.*, *61*, 2439–2448, doi:10.1063/1.1141336.

Sato, M., S. Yamamoto, Y. Yamamoto, Y. Okada, M. Ohno, H. Tsunakawa, and S. Maruyama (2015), Rock-magnetic properties of single zircon crystals sampled from the Tanzawa tonalitic pluton, central Japan, *Earth Planets Space*, *67*, 1–14, doi:10.1186/s40623-015-0317-9.

Stratton, J. A. (2007), *Electromagnetic Theory*, 640 pp., Wiley-IEEE Press, Hoboken, N. J.

Tarduno, J. A., R. D. Cottrell, W. J. Davis, F. Nimmo, and R. K. Bono (2015), A Hadean to Paleoarchean geodynamo recorded by single zircon crystals, *Science*, *349*, 521–524.

Uehara, M., and N. Nakamura (2006), Experimental constraints on magnetic stability of chondrules and the paleomagnetic significance of dusty olivines, *Earth Planet. Sci. Lett.*, *250*, 292–305.

Uehara, M., C. J. van der Beek, J. Gattacceca, V. A. Skidanov, and Y. Quesnel (2010), Advances in magneto-optical imaging applied to rock magnetism and paleomagnetism, *Geochem. Geophys. Geosyst.*, *11*, Q05Y09, doi:10.1029/2009GC002653.

Vestine, E. H., and N. Davids (1945), Analysis and interpretation of geomagnetic anomalies, *Terr. Magn. Atmos. Electr.*, *50*, 1–36.

Weiss, B. P., F. J. Baudenbacher, J. P. Wikswo, and J. L. Kirschvink (2001), Magnetic microscopy promises a leap in sensitivity and resolution, *Eos Trans. AGU*, *82*, 513–518, doi:10.1029/01EO00305.

Weiss, B. P., E. A. Lima, L. E. Fong, and F. J. Baudenbacher (2007a), Paleointensity of the Earth's magnetic field using SQUID microscopy, *Earth Planet. Sci. Lett.*, *264*, 61–71.

Weiss, B. P., E. A. Lima, L. E. Fong, and F. J. Baudenbacher (2007b), Paleomagnetic analysis using SQUID microscopy, *J. Geophys. Res.*, *112*, B09105, doi:10.1029/2007JB004940.

Weiss, B. P., L. E. Fong, H. Vali, E. A. Lima, and F. Baudenbacher (2008), Paleointensity of the ancient Martian magnetic field, *Geophys. Res. Lett.*, *35*, L23207, doi:10.1029/2008GL035585.

Weiss, B. P., S. Pedersen, I. Garrick-Bethell, S. T. Stewart, K. L. Louzada, A. C. Maloof, and N. L. Swanson-Hysell (2010), Paleomagnetism of impact spherules from Lonar crater, India and a test for impact-generated fields, *Earth Planet. Sci. Lett.*, *298*, 66–76.

Weiss, B. P., et al. (2015), Pervasive remagnetization of detrital zircon host rocks in the Jack Hills, Western Australia and implications for records of the early geodynamo, *Earth Planet. Sci. Lett.*, *430*, 115–128.

Weiss, B. P., A. C. Maloof, T. M. Harrison, N. L. Swanson-Hysell, R. R. Fu, J. L. Kirschvink, E. Bruce Watson, R. S. Coe, S. M. Tikoo, and J. Ramezani (2016), Reply to Comment on "Pervasive remagnetization of detrital zircon host rocks in the Jack Hills, Western Australia and implications for records of the early dynamo," *Earth Planet. Sci. Lett.*, *450*, 409–412, doi:10.1016/j.epsl.2016.07.001.

Wikswo, J. P., and K. R. Swinney (1985), Scalar multipole expansions and their dipole equivalents, *J. Appl. Phys.*, *57*, 4301–4308, doi: 10.1063/1.334589.

Yu, Y. (2010), Paleointensity determination using anhysteretic remanence and saturation isothermal remanence, *Geochem. Geophys. Geosyst.*, *11*, Q02Z12, doi:10.1029/2009GC002804.